

# 3D Field of Junctions: A Noise-Robust, Training-Free Structural Prior for Volumetric Inverse Problems

Namhoon Kim\*, Narges Moeini\*, Justin Romberg, and Sara Fridovich-Keil

Georgia Institute of Technology  
{namhoon@, nmoeini3@, jrom@ece., sfk@}gatech.edu

**Abstract.** Volume denoising is a foundational problem in computational imaging, as many 3D imaging inverse problems face high levels of measurement noise. Inspired by the strong 2D image denoising properties of Field of Junctions (ICCV 2021), we propose a novel, fully volumetric 3D Field of Junctions (3D FoJ) representation that optimizes a junction of 3D wedges that best explain each 3D patch of a full volume, while encouraging consistency between overlapping patches. In addition to direct volume denoising, we leverage our 3D FoJ representation as a structural prior that: (i) requires no training data, and thus precludes the risk of hallucination, (ii) preserves and enhances sharp edge and corner structures in 3D, even under low signal to noise ratio (SNR), and (iii) can be used as a drop-in denoising representation via projected or proximal gradient descent for any volumetric inverse problem with low SNR. We demonstrate successful volume reconstruction and denoising with 3D FoJ across three diverse 3D imaging tasks with low-SNR measurements: low-dose X-ray computed tomography (CT), cryogenic electron tomography (cryo-ET), and denoising point clouds such as those from lidar in adverse weather. Across these challenging low-SNR volumetric imaging problems, 3D FoJ outperforms a mixture of classical and neural methods.

**Keywords:** Volumetric denoising · Structural priors · Inverse problems · Tomography

## 1 Introduction

Denoising is a cornerstone of signal processing. While image denoising is well-studied, volume denoising remains an active research area as many modern computational imaging modalities are plagued by low signal to noise ratio (SNR), and denoising is a key step in many iterative algorithms for volumetric inverse problems. In medical imaging, including magnetic resonance imaging (MRI) and X-ray computed tomography (CT), low SNR can arise from using more accessible scanners with weaker magnetic fields [3], or by lowering the X-ray source intensity to reduce radiation exposure [19, 27]. In electron microscopy and tomography, low SNR is an inherent side effect of the low electron beam intensities

---

\* Equal contribution; order determined by coin flip.

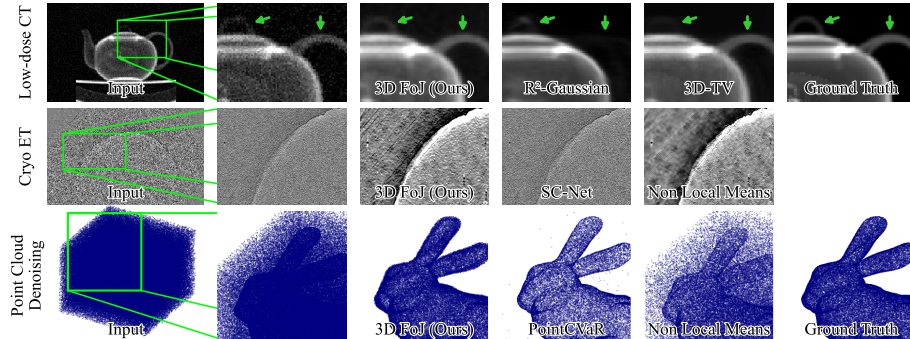


**Fig. 1:** Our 3D Field of Junctions (3D FoJ) is an effective volumetric denoiser across diverse inverse problems: low-dose computed tomography (*top row*), cryogenic electron tomography (*middle row*), and point cloud denoising (*bottom row*). Our cryo-ET experiment uses real data for which noiseless ground truth is not available. Only 3D FoJ successfully captures both the top and side handles of the teapot in low-dose CT.

necessary to avoid sample degradation [32]. In macro-scale 3D imaging, such as lidar used by autonomous vehicles, reconstructed point clouds suffer low SNR in adverse weather such as rain and snow [41].

Existing approaches to denoising often are not well-suited to 3D signals, require extensive training data, or struggle to resolve sharp boundary structure at low SNR. Classical structural and statistical priors [7, 37], and untrained neural networks like Deep Image Prior [33], Deep Decoder, [12], and implicit neural representations [25, 31], can effectively denoise volumes without any training data, but tend to blur edges and corners at low SNR. Data-driven priors including diffusion models [8, 36] can recover sharp signal structure, but require large training datasets and are thus often restricted to learning priors over 2D images [10] or small 3D patches [29] rather than full 3D volumes.

Inspired by Field of Junctions [34], a boundary-preserving optimization-based 2D image denoiser, we propose a novel 3D Field of Junctions (3D FoJ) representation, which extends similar principles for 3D volume denoising. Compared to the 2D Field of Junctions [34], our 3D FoJ (i) involves a significantly more intricate geometric formulation to operate natively in 3D, (ii) benefits from crucial engineering innovation that enables computational and memory efficiency even on high-resolution volumes, and (iii) can serve both as a direct volume denoiser and as a drop-in regularizer in diverse noisy 3D inverse problems, as shown in Figure 1.

3D FoJ works by parameterizing a volume as overlapping 3D patches, with each patch represented as a junction consisting of (i) a set of planes that divide the patch into 3D wedges, and (ii) a constant value inside each wedge. With this parameterization, by changing the positions of the planes and the values of the wedges, a 3D junction can exactly represent a sharp corner, straight or bent boundary, or constant region, and can approximate a curved boundary.

Hyper-parameters control the degree to which 3D FoJ penalizes sharp curvature. The junction parameters are optimized through a nonconvex yet empirically stable process that begins by greedily optimizing the parameters of each 3D patch individually in parallel, and then globally refines all junction parameters jointly by encouraging plane and wedge-value consistency across overlapping 3D patches. Together, the 3D FoJ parameterization and optimization process provide robust, boundary preserving volume denoising even under extremely low SNR.

To summarize, our contributions are:

- We introduce 3D Field of Junctions, an explicit, training-set-free structural prior for volumetric denoising and reconstruction in low-SNR 3D inverse problems.
- We formulate 3D FoJ for use in general noisy volume-reconstruction inverse problems via proximal gradient descent.
- We demonstrate 3D FoJ as a powerful and general-purpose denoiser across three diverse volumetric reconstruction and denoising tasks: low-dose CT, cryogenic electron tomography (cryo-ET), and point cloud denoising. Across these diverse tasks, 3D FoJ outperforms a variety of classical and neural denoisers and reconstruction methods.

Our implementation of 3D FoJ supports single and multi-GPU parallel processing of 3D patches and chunks of 3D patches to enable reconstruction and denoising of high-resolution volumes; code will be released in the near future.

## 2 Related Work

Many strategies have been proposed for volume denoising, broadly in the following categories.

*Classical denoising priors.* Classical structural priors such as bounded total variation (TV) [7], sparsity in a transform domain such as wavelet or discrete cosine transform (DCT) [22, 40], median filtering [37, 44], and nonlocal means filtering [5, 6, 11, 28] can be effective denoisers for both images and volumes. These require only a few hyper-parameters and no training data, and preserve edges better than  $\ell_2$  or Tikhonov regularization, but still suffer some loss of boundary structure under high noise. Our method is inspired by Field of Junctions [34], an explicit structural prior developed for robustly extracting sharp boundary structure in 2D images at low SNR. Our 3D FoJ applies similar principles to directly denoise low-SNR 3D volumes. In addition, we introduce an optimization framework that fits the model from *indirect* linear measurements, allowing it to be used as an implicit regularizer in inverse problem such as tomography ([34] requires an input noisy image rather than indirect noisy measurements of an image).

*Untrained neural priors.* Recently, neural networks have shown strong denoising capabilities. Untrained neural networks such as implicit neural representations (INRs) [24–26, 31], Deep Image Prior [33], and Deep Decoder [12] leverage the architectural restrictions of a neural network as a form of implicit regularization that can remove high-frequency noise through restricting model size or training time [13]. We refer to these methods as “untrained” because the model parameters are optimized to fit each signal separately, with no larger training dataset. Like their classical counterparts, untrained neural networks can be effective denoisers and require no training data, but suffer loss of boundary structure at very low SNR.

*Data-driven neural priors.* Trained deep network denoisers can learn complex statistical features of a training dataset, allowing them to preserve edge structure even under high noise [14, 15, 43, 45]. However, such models require large training datasets of clean [8, 36] and/or noisy examples [1, 18], that are often prohibitive to collect for 3D signals. While denoisers trained on 2D signals [9, 10, 17] or small 3D patches [29] can be retroactively applied to denoise a 3D volume, these applications are approximate and some 3D structure is often lost.

### 3 Preliminaries: 2D Field of Junctions

The Field of Junctions model [34] provides a unified framework for representing contours, corners, and multi-way junctions in 2D images, and robustly extracts this boundary structure even under low SNR. FoJ models each image patch with a parametric *M-junction*, a configuration of  $M$  wedges meeting at a freely located vertex, that captures local boundary geometry within a small neighborhood. Let  $I : \Omega \rightarrow \mathbb{R}^K$  denote a  $K$ -channel image (*e.g.*,  $K=1$  for grayscale), where  $\Omega \subset \mathbb{R}^2$  is the image domain. The image  $I$  is divided into overlapping patches  $\{I_i\}_{i=1}^N$  of size  $R \times R$ , with stride  $s$  in each dimension. For the  $i$ th patch, the junction parameters are

$$\boldsymbol{\theta}_i = (\phi_i, \mathbf{p}_i^{(0)}), \quad \phi_i = (\phi_i^{(1)}, \dots, \phi_i^{(M)}), \quad (1)$$

where  $\phi_i^{(k)}$  denotes the orientation of the  $k$ th boundary, and  $\mathbf{p}_i^{(0)} = (x_i^{(0)}, y_i^{(0)})$  is the vertex position, which may lie inside or outside the patch. The number of wedges  $M$  determines the local boundary complexity: for example, when  $M=3$ , the model captures three intersecting lines that can form T- or Y-junctions, but can also model straight or bent edges or uniform regions when one or more lines coincide (see Figure 2(a)). Each wedge  $j$  in junction  $i$  is also endowed with a constant (optimizable) color value  $c_i^{(j)} \in \mathbb{R}^K$ .

The junction parameters  $\Theta = \{\boldsymbol{\theta}_i\}$  and colors  $C = \{c_i^{(j)}\}$  are estimated by minimizing a global objective that enforces both patch fidelity and inter-patch consistency:

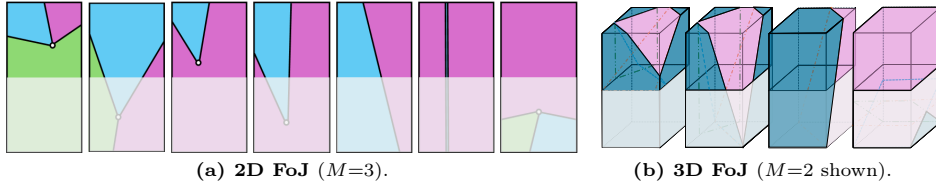


**Fig. 2: Junction schematics for Field of Junctions (FoJ) in 2D (left) and our 3D FoJ (right).** (a) In 2D, [34] models each patch as an  $M$ -junction: a vertex and  $M$  angles define  $M$  uniform-color wedges. Allowing the vertex to lie inside or outside the patch enables a unified representation of edges, corners, junctions, and homogeneous regions. (b) In 3D, we visualize the two-region case ( $M=2$ ) with different configurations of intersecting planes inside a volumetric patch. We show  $M=2$  for visual clarity; our experiments use  $M=3$  regions.

$$\begin{aligned} \arg \min_{\Theta, C} \quad & \sum_{i,j} \iint u_{\theta_i}^{(j)}(\mathbf{p}) \|I_i(\mathbf{p}) - c_i^{(j)}\|^2 d\mathbf{p} + \lambda_B \sum_i \iint_{\Omega_i} [B_i(\mathbf{p}) - \hat{B}(\mathbf{p})]^2 d\mathbf{p} \\ & + \lambda_C \sum_{i,j} \iint u_{\theta_i}^{(j)}(\mathbf{p}) \|c_i^{(j)} - \hat{I}(\mathbf{p})\|^2 d\mathbf{p}. \end{aligned} \quad (2)$$

Here,  $I_i(\mathbf{p})$  denotes the observed (noisy) image within patch  $i$  with domain  $\Omega_i$ , and  $c_i^{(j)}$  is the constant color associated with wedge  $j$  inside junction  $i$ . The first term of Equation (2) enforces fidelity between each observed image patch and its piecewise-constant junction representation. The second term, weighted by  $\lambda_B \geq 0$ , aligns boundary locations among neighboring patches through the local and global boundary maps  $B_i(\mathbf{p})$  and  $\hat{B}(\mathbf{p})$ , respectively. The local map  $B_i(\mathbf{p})$  equals 1 at pixels lying on the boundaries defined by  $\theta_i$ , and 0 elsewhere, while the global map  $\hat{B}(\mathbf{p})$  is obtained by averaging all overlapping local boundary maps across patches. The third term, weighted by  $\lambda_C \geq 0$ , enforces consistent regional appearance by comparing each patch’s color estimate with the global color field  $\hat{I}(\mathbf{p})$ , which averages the reconstructed intensities of all patches covering the same pixel. For optimization, the binary wedge indicator functions  $u_{\theta_i}^{(j)}(\mathbf{p})$  and boundary maps  $B_i(\mathbf{p})$  are replaced by smooth, differentiable approximations to enable gradient-based refinement; these differentiable formulations are detailed in the appendix.

## 4 Method: 3D Field of Junctions

Our 3D FoJ is inspired by 2D Field of Junctions (FoJ) [34] but operates natively in 3D for volumetric signals. FoJ models image patches as junctions parameterized by intersecting lines and constant-color wedges. In three dimensions, we generalize these boundaries to planar surfaces that divide a 3D patch into

constant-value regions. Like its 2D counterpart, our 3D FoJ uses a unified junction parameterization model to represent 3D patches with many possible shapes, including constant regions, straight and bent edges, and multi-surface junctions.

#### 4.1 Local Volumetric Model

Each volumetric patch  $V_i : \Omega_i \rightarrow \mathbb{R}^K$  is modeled as a 3D region partitioned by three planes that intersect at a common vertex  $\mathbf{v}_i^{(0)} \in \mathbb{R}^3$ , which may lie inside or outside the 3D patch. Here,  $\Omega_i \subset \mathbb{R}^3$  denotes the spatial domain of the 3D patch. The full 3D volume is divided into overlapping patches  $\{V_i\}_{i=1}^N$ , each of size  $R \times R \times R$ , with stride  $s$  in each dimension. Each voxel intensity is represented as a  $K$ -dimensional vector (*e.g.*,  $K=1$  for grayscale data). The parameters of junction  $i$  are defined as

$$\boldsymbol{\gamma}_i = (\boldsymbol{\rho}_i^{(\ell)}, \mathbf{v}_i^{(0)}), \quad \boldsymbol{\rho}_i^{(\ell)} = (\theta_i^{(\ell)}, \phi_i^{(\ell)}), \quad \ell = 1, 2, 3 \quad (3)$$

where each pair  $(\theta_i^{(\ell)}, \phi_i^{(\ell)})$  specifies the polar and azimuthal angles of the  $\ell$ th plane normal, and  $\mathbf{v}_i^{(0)} = (x_i^{(0)}, y_i^{(0)}, z_i^{(0)})$  denotes the vertex position at which the three planes intersect. Since the vertex may freely move inside or outside the 3D patch, the junction can represent a wide variety of 3D structures as illustrated in Figure 2b. The three planes divide each patch into regions (generalized 3D wedges), each of which is modeled with a constant parameter value (intensity, color, density, etc.)  $c_i^{(j)} \in \mathbb{R}^K$ .

#### 4.2 Global Objective Function

We jointly optimize the parameters  $\Gamma = (\boldsymbol{\gamma}_1, \dots, \boldsymbol{\gamma}_N)$  and regional intensities  $C = (c_1, \dots, c_N)$  to minimize a global objective that enforces both local data fidelity and inter-patch coherence across the entire volume. Our volumetric extension of the 2D FoJ objective is given by:

$$\begin{aligned} \min_{\Gamma, C} \quad & \sum_{i,j} \iiint u_{\boldsymbol{\gamma}_i}^{(j)}(\mathbf{v}) \|V_i(\mathbf{v}) - c_i^{(j)}\|^2 d\mathbf{v} + \lambda_B \sum_i \iiint_{\Omega_i} [B_i(\mathbf{v}) - \widehat{B}(\mathbf{v})]^2 d\mathbf{v} \\ & + \lambda_C \sum_{i,j} \iiint u_{\boldsymbol{\gamma}_i}^{(j)}(\mathbf{v}) \|c_i^{(j)} - \widehat{V}(\mathbf{v})\|^2 d\mathbf{v}. \end{aligned} \quad (4)$$

Here,  $u_{\boldsymbol{\gamma}_i}^{(j)}(\mathbf{v}) \in \{0, 1\}$  denotes membership of a voxel  $\mathbf{v} = (x, y, z)$  in the  $j$ th volumetric region of patch  $i$ ,  $V_i(\mathbf{v})$  represents the observed volume within patch  $i$  (with domain  $\Omega_i$ ), and  $c_i^{(j)}$  is the constant value associated with region  $j$  of the junction model for patch  $i$ . The first term enforces local reconstruction accuracy of each patch using its piecewise-constant junction model. The second term, weighted by  $\lambda_B \geq 0$ , aligns local and global boundary estimates through the boundary fields  $B_i(\mathbf{v})$  and  $\widehat{B}(\mathbf{v})$ , which will be defined shortly in the *Global Maps* paragraph. This term encourages continuity of surface structures across overlapping patches. The third term, weighted by  $\lambda_C \geq 0$ , promotes consistent regional appearance by comparing each patch's reconstructed intensity to the global field  $\widehat{V}(\mathbf{v})$  obtained by averaging overlapping patch reconstructions.

*Global Maps.* The global volumetric color and boundary fields are defined by aggregating the contributions of all patches that contain a given voxel  $\mathbf{v}$ . The global color field  $\widehat{V}(\mathbf{v})$  is given by

$$\widehat{V}(\mathbf{v}) = \frac{1}{|\mathcal{N}_{\mathbf{v}}|} \sum_{i \in \mathcal{N}_{\mathbf{v}}} \sum_{j=1}^M u_{\gamma_i}^{(j)}(\mathbf{v}) c_i^{(j)}, \quad (5)$$

where  $\mathcal{N}_{\mathbf{v}}$  denotes the set of all patches that include voxel  $\mathbf{v}$ , and  $|\mathcal{N}_{\mathbf{v}}|$  is its cardinality, the number of patches that include voxel  $\mathbf{v}$ . This operation computes a weighted average of all region intensities overlapping at  $\mathbf{v}$ , yielding a smooth global volume reconstruction. Similarly, the relaxed global boundary field  $\widehat{B}(\mathbf{v})$  averages local boundary predictions from all overlapping patches:

$$\widehat{B}(\mathbf{v}) = \frac{1}{|\mathcal{N}_{\mathbf{v}}|} \sum_{i \in \mathcal{N}_{\mathbf{v}}} B_i(\mathbf{v}), \quad (6)$$

where  $B_i(\mathbf{v}) \in \{0, 1\}$ . This field encodes the presence or absence of a boundary plane at each voxel, effectively representing the local boundary consensus across overlapping patches. Although the binary formulation provides a clear geometric interpretation, it is not differentiable and therefore unsuitable for gradient-based optimization. To enable efficient and stable optimization of the junction parameters  $\gamma_i$ , we replace the binary region indicators and boundary maps with differentiable, smooth counterparts, introduced in the following subsection.

### 4.3 Smooth Indicator Functions

To enable gradient-based optimization, the region indicator functions in Equation (2) must be differentiable. We therefore define soft indicator functions using signed distance values relative to the three separating planes of each 3D patch. For voxel  $\mathbf{v} = (x, y, z)$ , the signed distance to the  $\ell$ th plane is given by

$$d_{\ell}(\mathbf{v}) = \langle (x, y, z) - (x_i^{(0)}, y_i^{(0)}, z_i^{(0)}), \mathbf{n}_i^{(\ell)} \rangle, \quad (7)$$

where  $\mathbf{n}_i^{(\ell)}$  is the normal vector of the  $\ell$ th plane, parameterized by its polar and azimuthal angles  $(\theta_i^{(\ell)}, \phi_i^{(\ell)})$ . Inspired by the 2D FoJ formulation [34], we use a Heaviside function as a differentiable approximation of the binary region assignment  $H_{\eta}(d) = \frac{1}{2} \left( 1 + \frac{2}{\pi} \arctan \frac{d}{\eta} \right)$ , where  $\eta > 0$  controls the transition sharpness across the plane boundaries. The differentiable volumetric region indicators are then defined as

$$\begin{aligned} u_{\gamma_i}^{(1)}(\mathbf{v}) &= H_{\eta}(d_1(\mathbf{v})) [1 - H_{\eta}(d_2(\mathbf{v}))] [1 - H_{\eta}(d_3(\mathbf{v}))], \\ u_{\gamma_i}^{(2)}(\mathbf{v}) &= [1 - H_{\eta}(d_1(\mathbf{v}))] H_{\eta}(d_2(\mathbf{v})) [1 - H_{\eta}(d_3(\mathbf{v}))], \\ u_{\gamma_i}^{(3)}(\mathbf{v}) &= [1 - H_{\eta}(d_1(\mathbf{v}))] [1 - H_{\eta}(d_2(\mathbf{v}))] H_{\eta}(d_3(\mathbf{v})), \end{aligned} \quad (8)$$

for our parameterization with 3 regions per patch. By following a similar pattern

and enumerating over all 8 binary arrangements with 3 planes, our 3D junction model can represent up to 8 distinct regions per 3D patch. These functions softly assign each voxel to one of these three regions based on its position relative to the planes, providing continuous gradients for optimization.

We note that partitioning a 3D patch into  $M$  disjoint regions is more geometrically complex than partitioning a 2D patch. Our 3D FoJ formulation based on three intersecting planes naturally divides a 3D patch into eight regions; we work with fewer (typically  $M = 3$ ) regions by only assigning nonzero values to a subset of these eight regions. In particular, the region assignments in Equation (8) may leave some portion of the patch outside any of the  $M = 3$  regions and thus with default value zero. Effectively we find that these zero-valued regions do not negatively impact reconstruction or denoising quality; we use  $M = 3$  in our experiments to balance the expressivity of having more regions per junction with the increased computational and memory cost. Ablation studies over the choice of  $M$  are provided in Table 3 and Table 7.

*Smooth Boundary Map.* To compare and align local surfaces across overlapping patches, we use a differentiable boundary-strength field from the 2D FoJ formulation [34]:

$$B_i^{(\delta)}(\mathbf{v}) = \pi \delta H'_\delta\left(\min_{i \in \{1,2,3\}} \{|d_i(\mathbf{v})|\}\right) \in [0, 1]. \quad (9)$$

Here  $H_\delta(d)$  is the regularized Heaviside function and  $H'_\delta(d)$  is its derivative with respect to  $d$ . The input  $d$  to  $H'_\delta$  is the distance of voxel  $\mathbf{v}$  to the nearest separating plane; thus  $B_i^{(\delta)}(\mathbf{v})$  attains high values near predicted surfaces and smoothly decays with distance. The parameter  $\delta > 0$  controls the transition width: larger  $\delta$  yields broader, softer boundaries; smaller  $\delta$  produces sharper peaks. This soft boundary field serves as a differentiable surrogate for a binary boundary map, and is used in the boundary-consistency term of Equation (4) to encourage inter-patch alignment of boundary planes.

#### 4.4 Optimization Procedure

Reconstructing the volumetric Field of Junctions involves minimizing a non-convex objective over the 3D junction parameters  $\gamma_i = (\boldsymbol{\rho}_i, \mathbf{v}_i^{(0)})$ . Similar to the 2D case [34], we perform this nonconvex optimization in two stages: an initialization stage that estimates local geometry for each patch independently, and a refinement stage that jointly optimizes all patches using differentiable indicator functions. A detailed step-by-step version of this optimization process is provided in the Appendix.

*Initialization Step.* The initialization stage provides a coarse yet reliable estimate of the plane orientations and their vertex positions within each patch. Each junction is initialized with the vertex  $\mathbf{v}_i^{(0)}$  placed at the center of the patch, and the plane orientation parameters  $\boldsymbol{\rho}_i^{(\ell)} = (\theta_i^{(\ell)}, \phi_i^{(\ell)})$  are optimized using a discrete coordinate-descent search. For each orientation pair  $(\theta, \phi)$ , the data

fidelity term from Equation (4) is evaluated over a uniform angular grid, and the minimizing direction is selected. After the optimal plane orientations are estimated, the vertex position  $\mathbf{v}_i^{(0)} = (x_i^{(0)}, y_i^{(0)}, z_i^{(0)})$  is refined by scanning a small neighborhood around its current position to minimize the same data term. This coordinate-wise update is repeated cyclically across the vertex and all planes until convergence, defined by a fixed number of iterations. This procedure is robust to noise and computationally efficient, as all patches can be processed in parallel.

*Refinement Step.* After initialization, all patches are jointly refined using gradient-based optimization of the full objective function in Equation (4). The binary region indicators and boundary maps are replaced by their differentiable counterparts (defined in Section 4.3), enabling end-to-end optimization through the junction parameters  $\gamma_i$ . We use first-order iterative optimization (e.g., Adam) to update  $\theta_i^{(\ell)}$ ,  $\phi_i^{(\ell)}$ , and  $\mathbf{v}_i^{(0)}$ , while the region intensities  $c_i^{(j)}$  are updated analytically at each iteration using the following closed-form solution:

$$c_i^{(j)} = \frac{\iiint u_{\gamma_i}^{(j)}(\mathbf{v}) [V_i(\mathbf{v}) + \lambda_C \widehat{V}(\mathbf{v})] d\mathbf{v}}{(1 + \lambda_C) \iiint u_{\gamma_i}^{(j)}(\mathbf{v}) d\mathbf{v}}. \quad (10)$$

During refinement, the regularization weights  $\lambda_B$  and  $\lambda_C$  are gradually increased from small initial values to their final targets, ensuring stable convergence and avoiding premature over-smoothing. This joint optimization progressively improves both the geometric accuracy of the surfaces and their spatial consistency across overlapping patches, yielding a coherent 3D Field of Junctions.

#### 4.5 Solving Inverse Problems with 3D FoJ

Our 3D FoJ model can be used as a drop-in structural prior in any volumetric inverse problem; we showcase it in the context of low-dose sparse-view tomographic reconstruction. The reconstruction problem is formulated as

$$\min_{\mathbf{x}} f(\mathbf{x}) + g(\mathbf{x}), \quad (11)$$

where  $\mathbf{x} \in \mathbb{R}^{D \times H \times W \times K}$  denotes the volumetric image to be reconstructed. The data fidelity term  $f(\mathbf{x})$  encourages consistency with the measured projections:

$$f(\mathbf{x}) = \frac{1}{2} \|\mathbf{A}\mathbf{x} - \mathbf{b}\|^2, \quad (12)$$

where  $\mathbf{A}$  is the system matrix (for tomography, the Radon transform) and  $\mathbf{b}$  is the vector of projection measurements. The 3D FoJ regularization term

$$g(\mathbf{x}) = \min_{\Gamma, C} \|\mathbf{x} - R(\Gamma, C)\|^2 \quad (13)$$

encourages geometric consistency in voxel space, with  $R(\Gamma, C)$  denoting the reconstructed volume parameterized by 3D FoJ parameters  $\Gamma$  and  $C$ . We solve Equation (11) via a proximal-gradient method:

$$\mathbf{x}^{(k+1)} = \text{prox}_{\lambda g} \left( \mathbf{x}^{(k)} - \lambda \nabla f(\mathbf{x}^{(k)}) \right), \quad (14)$$

which alternates between a gradient descent step on the data term and a proximal step defined by the FoJ prior. The scalar  $\lambda > 0$  serves a dual role: it acts as the gradient descent step size on the data fidelity term  $f(\mathbf{x})$ , and simultaneously controls the strength of the 3D FoJ regularization through the proximal operator. As  $\lambda \downarrow 0$ , the update approaches a pure gradient descent step with negligible 3D FoJ influence, and the reconstruction converges toward the conventional least-squares solution. Conversely, as  $\lambda \uparrow \infty$ , the proximal step dominates and the solution is driven toward the 3D FoJ manifold, yielding reconstructions that closely follow the 3D FoJ structural prior  $R(I, C)$ . In practice,  $\lambda$  is tuned to balance data fidelity and 3D FoJ regularization. The two updates can be written explicitly as:

$$\mathbf{x}^{(k+\frac{1}{2})} = \mathbf{x}^{(k)} - \lambda \nabla f(\mathbf{x}^{(k)}). \quad (15)$$

$$\mathbf{x}^{(k+1)} = \arg \min_{\mathbf{x}} \left[ g(\mathbf{x}) + \frac{1}{2\lambda} \|\mathbf{x} - \mathbf{x}^{(k+\frac{1}{2})}\|^2 \right]. \quad (16)$$

The first half-iteration (Equation (15)) corresponds to a conventional gradient descent update enforcing data consistency, and the second half-iteration (Equation (16)) approximates this proximal step efficiently by performing a single 3D FoJ update (one iteration of the initialization step and one iteration of the refinement step) per outer iteration, initialized from the intermediate volume. In practice, a single FoJ update at each proximal step is sufficient to guide the solution toward the FoJ manifold while keeping the overall reconstruction computationally tractable. This proximal formulation enables joint recovery of the voxel intensity field and the underlying junction geometry within each iteration, using noisy tomographic measurements rather than direct access to a noisy volume. We emphasize that, while we present results on a tomographic inverse problem, the same proximal gradient formulation would enable 3D FoJ to be used as a drop-in structural prior to regularize any volumetric inverse problem.

## 5 Results

To illustrate the broad applicability of 3D FoJ as a structural prior for volume reconstruction and denoising, we perform experiments on three diverse volume imaging tasks that share the key feature of inherent measurement noise: low-dose X-ray computed tomography (CT), cryogenic electron tomography (cryo-ET), and point cloud denoising. Low-dose CT and cryo-ET face severe shot noise due to low X-ray and electron beam intensities, which are restricted to avoid radiative damage and sample degradation, respectively. Point clouds reconstructed from sensors such as lidar can be corrupted by outliers due to sensor noise or adverse weather. Our experiments frame X-ray CT as an inverse problem, where we use 3D FoJ inside proximal gradient descent to reconstruct a denoised volume from raw noisy projections. For cryo-ET and point cloud denoising, we start with a noisy volume and showcase 3D FoJ as a direct 3D denoiser.

### 5.1 Low-dose X-ray Computed Tomography (CT)

To evaluate the reconstruction performance of our 3D FoJ for limited-angle and low-dose 3D CT reconstruction, we conduct experiments on five synthetic volumetric datasets—*pepper*, *teapot*, *jaw*, *foot*, and *engine*—originally introduced in the R<sup>2</sup>-Gaussian paper [42]. We reconstruct each object from 20 non-uniform projection angles, each with an image size of  $256 \times 256$ . To emulate low-dose X-ray acquisition, we add Poisson-distributed noise to the synthetic projection data, where the simulated photon count per detector pixel determines the effective signal-to-noise ratio (SNR).

We simulate three photon-count levels, denoted as *P50*,

*P100*, and *P1000*, corresponding respectively to increasing SNR regimes. Here, the notation *Pn* indicates an expected photon count of *n* per pixel, with *P50* representing the lowest SNR (extreme noise) and *P1000* representing the highest SNR (but still noisy) condition. Additional qualitative comparisons of unseen projection views (Figures 6 to 8) and reconstructed axial, sagittal, and coronal slice views (Figures 9 to 11) across all datasets and noise levels further demonstrate the consistent structural fidelity and noise robustness of 3D FoJ.

We compare our 3D FoJ reconstructions against several baselines, including R<sup>2</sup>-Gaussian [42], Filter2Noise [30], and 3D total variation (TV) regularization [4]. We evaluate reconstruction fidelity using both volumetric and projection-based metrics. Specifically, we report the 3D peak signal-to-noise ratio (3D PSNR) computed on the reconstructed volumes and the multi-scale structural similarity (MS-SSIM) [35] measured on 360 2D projections (one per degree along a circular trajectory). Table 1 summarizes the average MS-SSIM and 3D PSNR across all

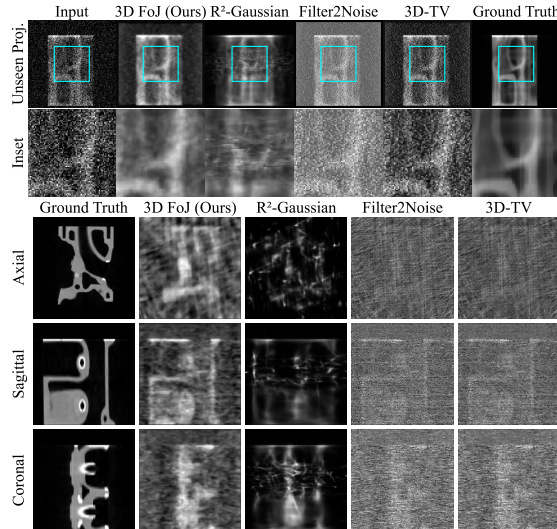


**Fig. 3:** Comparison of unseen projection views synthesized from reconstructed 3D volumes (top) and slice views of reconstructed 3D volumes (bottom) for the *engine* dataset under low-SNR (*P50*) conditions.

Metric	Method	P50	P100	P1000
2D MS-SSIM	3D-TV	0.703	0.739	0.829
	R <sup>2</sup> -Gaussian	0.574	0.577	0.652
	Filter2Noise	0.663	0.689	0.695
	3D FoJ (ours)	0.754	0.788	0.838
3D PSNR	3D-TV	13.79	15.31	16.96
	R <sup>2</sup> -Gaussian	15.29	15.29	15.87
	Filter2Noise	11.61	15.13	14.64
	3D FoJ (ours)	15.88	16.14	16.72

**Table 1:** Average MS-SSIM on 2D projections (360 views) and 3D PSNR on volumes across all CT datasets (*engine*, *foot*, *jaw*, *pepper*, and *teapot*) for each noise level. 3D FoJ performs best, especially at low SNR.

datasets (*engine*, *foot*, *jaw*, *pepper*, and *teapot*) and noise levels. As shown, 3D FoJ consistently achieves the highest reconstruction fidelity across all noise levels, with a particularly substantial improvement under low-SNR (low photon count) conditions. The Figure 3 provides qualitative comparisons of the reconstructed geometry under the low-SNR ( $P50$ ) condition. The top row shows an unseen projection synthesized from each reconstructed 3D volume, which tests global consistency for a view not included in the input angles. The bottom row shows slice views of the reconstructed volumes, where 3D FoJ preserves cleaner surfaces, sharper edges, and more faithful structural details than all baselines. The full quantitative comparison across all datasets and noise levels, including both projection-based MS-SSIM and volumetric 3D PSNR metrics, is provided in the Appendix Table 4.

## 5.2 Cryogenic Electron Tomography (cryo-ET)

To evaluate the denoising capability of our method on real-world electron microscopy data, we conducted experiments on four cryo-ET datasets: *centriole* from [16] and *mitochondria*, *vesicle*, and *VEEV* from [39]. We take as input the noisy volumes re-

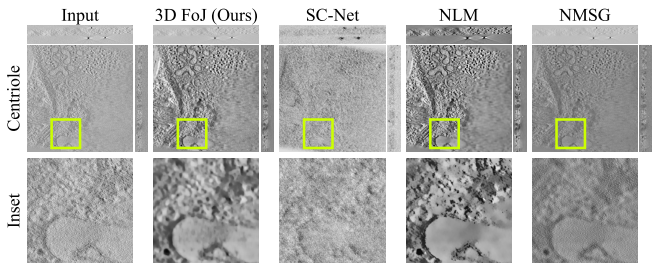


**Fig. 4:** Visual denoising results for the real cryo-ET *centriole* volume, sliced in each dimension. 3D FoJ preserves fine structural details that are overly smoothed by NLM.

constructed using the `tilt` program in IMOD [16] as described in the SC-Net pipeline [39]. Noise in the input volumes is the result of both electron shot noise, because the electron beam intensity is limited to avoid sample degradation, and missing wedge artifacts, because cryo-ET projections are geometrically constrained to measure limited angles.

As ground truth noiseless volumes are unavailable for these real world datasets, in Figure 4 we provide a qualitative visual comparison of reconstruction quality. We compared our 3D FoJ method against SC-Net [39], Noise Modeling and Sparsity Guidance (NMSG) [38], and nonlocal means denoising (NLM) [5] as representative neural [38, 39] and classical [5] denoisers applicable to cryo-ET volumes. Qualitative volume denoising results in Figure 4 show that 3D FoJ achieves the best balance of denoising, contrast enhancement, and detail preservation. Further qualitative results on real cryo-ET volumes are presented in the Appendix (Figure 12), illustrating the denoising performance of 3D FoJ relative to competing approaches.

## 5.3 Point Cloud Denoising

We further evaluate our method on point cloud denoising tasks, using a total of 28 point clouds provided by PointCleanNet [23]. We consider two noise models:

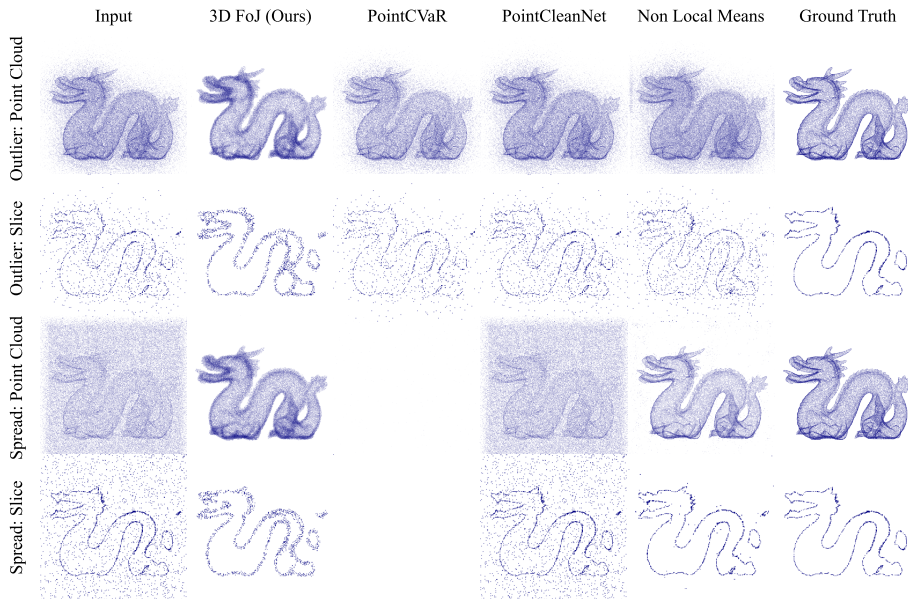


**Fig. 5:** Denoising results for the *dragon* point cloud with 60% *outlier* noise and 500k random *spread* points. Slices show that 3D FoJ effectively removes noise both inside and outside the object surface. At this extreme level of *spread* noise, PointCVaR rejects nearly all points as outliers.

(i) outlier noise modeled on what might be expected from lidar sensor noise or miscalibration, in which noise points are concentrated near object surfaces, and (ii) synthetic real-world noise similar to what would be expected from a lidar sensor in rain or snow. We refer to the first noise model as *outlier* and the second as *spread*. Our *outlier* removal experiments use the same noise configurations as PointCleanNet [23], focusing on the four outlier ratios (10%, 30%, 60%, 90%) in their dataset. Our *spread* denoising experiments use simulated inclement-weather lidar noise modeled on a similar experiment from PointCleanNet. For each point cloud, we randomly add 40k, 100k, 200k, or 500k noisy points within an axis-aligned bounding box, defined by padding along each of the  $x$ ,  $y$ , and  $z$  axes by 10 meters.

We compare our 3D FoJ method against PointCleanNet [23], PointCVaR [21], and nonlocal means (NLM) [5] as representative strong and diverse baselines for point cloud denoising. PointCleanNet uses a neural network for denoising, PointCVaR follows a statistical approach to reject outlier points, and nonlocal means averages structurally similar but disjoint 3D patches to reduce noise. Because 3D

Task Level	PointCVaR	PointCleanNet	NLM	3D FoJ (Ours)
Outlier	10%	2.15 ± 6.47	2.17 ± 6.44	5.02 ± 16.73
	30%	6.54 ± 19.39	6.52 ± 19.25	7.82 ± 24.15
	60%	12.93 ± 38.26	12.98 ± 38.19	13.41 ± 40.62
	90%	19.64 ± 57.82	19.57 ± 57.56	18.35 ± 54.88
Spread	40k	154.41 ± 396.20	62.33 ± 191.76	87.05 ± 279.53
	100k	0.44 ± 0.66	108.50 ± 333.13	138.14 ± 438.95
	200k	256.72 ± 661.88	144.94 ± 445.71	168.08 ± 527.55
	500k	515.25 ± 1327.14	181.12 ± 557.22	102.84 ± 334.54

**Table 2:** Point cloud denoising (Chamfer-L2), mean±std across shapes. Best per level is highlighted. PointCVaR is competitive at moderate spread noise but is less robust across noise levels.

FoJ and NLM are configured for voxel rather than point cloud denoising, for these methods we convert the noisy input point cloud into a  $256^3$  voxel grid before denoising. After denoising, we convert the results from these voxel-based methods (3D FoJ and NLM) back into point clouds by placing points at the highest-intensity 100k voxel coordinates, to match the point-based denoisers (PointCleanNet and PointCVaR) which are configured to output 100k points. We report Chamfer Distance (CD) [2, 20] in Table 2 to quantify geometric consistency between denoised and ground truth point clouds. We find that 3D FoJ is a robust point cloud denoiser for both types of noise and across all noise levels, extracting robust shape structure even under low SNR. Visual results are shown in Figure 5. Additional quantitative evaluations under impulse noise and spread noise settings are reported in the Appendix (Tables 5 and 6), further demonstrating the robustness and consistency of 3D FoJ across a wide range of outlier corruption levels.

#### 5.4 Ablation Study

We perform an ablation study on the *engine* CT dataset at the lowest SNR level (P50), to assess the influence of patch size, stride, batch size, and number of regions on reconstruction quality. For this experiment, we first reconstruct the 3D volume from its sparse, noisy projections using the standard CGLS algorithm, and then fit 3D FoJ to the resulting volume under different parameter configurations.

# regions	Batch size	Stride	Patch size	MS-SSIM	3D PSNR	Runtime
3	6	1	4	0.755	11.84	14.3 min
3	6	1	6	0.732	14.29	31.6 min
3	6	1	8	0.722	15.76	47.3 min
3	6	2	4	0.762	11.33	7.2 min
3	6	2	6	0.784	14.37	10.5 min
3	6	2	8	0.796	16.18	13.1 min
3	6	2	10	0.798	17.17	17.2 min
3	6	2	12	0.800	17.70	24.7 min
3	1	2	10	0.798	17.17	37.6 min
3	2	2	10	0.798	17.17	25.6 min
3	3	2	10	0.798	17.17	24.5 min
3	4	2	10	0.798	17.17	20.3 min
3	5	2	10	0.798	17.17	18.5 min
3	6	2	10	0.798	17.17	17.2 min
2	6	2	10	0.805	17.03	15.2 min
3	6	2	10	0.798	17.17	17.2 min
4	6	2	10	0.798	16.70	20.3 min
5	6	2	10	0.797	16.43	21.5 min
6	6	2	10	0.790	16.50	22.8 min
7	6	2	10	0.799	16.37	25.1 min
8	6	2	10	0.797	16.12	27.7 min

**Table 3:** Ablation study over 3D FoJ hyperparameters on the *engine* CT dataset at noise level (P50).

Results are reported in Table 3. Increasing the patch size generally improves reconstruction quality (higher MS-SSIM and 3D PSNR) in low-SNR settings, but at the cost of increased runtime. We expect that the optimal patch size is likely an increasing function of noise level, as larger patches can average out more noise.

Using a stride of 2 achieves a favorable trade-off between reconstruction fidelity and efficiency; slightly higher fidelity is possible with a stride of 1, but at a substantial computational price.

The batch size for parallel processing primarily affects runtime, with no impact on reconstruction accuracy. Varying the number of regions per junction shows that using two or three regions provides the best balance of reconstruction quality and speed.

It is possible that higher junction complexity could prove beneficial for particularly complex structures, or with additional steps of refinement optimization.

Our default configuration uses a patch size of 10, stride of 2, batch size of 6, and  $M = 3$  regions per junction.

The complete set of ablation results, including additional configurations for initialization and refinement iterations as well as detailed runtime comparisons, is provided in the Appendix Table 7 and Figure 13.

## 6 Discussion

Our experiments confirm that our proposed 3D Field of Junctions parameterization is an effective prior for 3D denoising and noisy volumetric inverse problems, capable of extracting sharp boundary structure in 3D even under extremely low SNR. We emphasize that 3D FoJ is fully explicit, with all parameters endowed with physical structural interpretation. It requires neither training data nor neural networks, can run on a single GPU or parallelize across several, and has fairly stable performance across hyperparameter settings and noise levels. It robustly extracts 3D structure across different types of noise, and works well in both direct volume denoising and indirect regularization of low-SNR volumetric inverse problems, outperforming both classical and neural alternatives.

Our results are subject to two main limitations. First, we did not tune the various 3D FoJ hyperparameters (patch size, stride, number of regions  $M$  per patch, or the smoothness parameters  $\eta$  and  $\delta$ ) separately for each task. While this ensures our results reflect expected performance on new tasks, stronger performance is likely possible with additional hyperparameter tuning, especially for different noise levels and dataset resolutions. The other limitation of 3D FoJ is its computational cost. For a moderate-size volume ( $256^3$ ), fitting a 3D FoJ model runs in a few minutes on an A6000 GPU (48 GB RAM). However, memory usage increases with both patch and volume size, necessitating parallel processing (which our code supports) for large cases.

## References

1. Aali, A., Arvinte, M., Kumar, S., Tamir, J.I.: Solving inverse problems with score-based generative priors learned from noisy data. In: 2023 57th Asilomar Conference on Signals, Systems, and Computers. pp. 837–843 (2023). <https://doi.org/10.1109/IEEECONF59524.2023.10477042>
2. Achlioptas, P., Diamanti, O., Mitliagkas, I., Guibas, L.: Learning representations and generative models for 3d point clouds. In: International conference on machine learning. pp. 40–49. PMLR (2018)
3. Arnold, T.C., Freeman, C.W., Litt, B., Stein, J.M.: Low-field mri: clinical promise and challenges. *Journal of Magnetic Resonance Imaging* **57**(1), 25–44 (2023)
4. Barbero, A., Sra, S.: Modular proximal optimization for multidimensional total-variation regularization. *Journal of Machine Learning Research* **19**(56), 1–82 (2018), <http://jmlr.org/papers/v19/13-538.html>
5. Bruns, S., Stipp, S., Sørensen, H.: Looking for the signal: A guide to iterative noise and artefact removal in x-ray tomographic reconstructions of porous geomaterials. *Advances in Water Resources* **105**, 96–107 (2017)
6. Buades, A., Coll, B., Morel, J.M.: A review of image denoising algorithms, with a new one. *Multiscale modeling & simulation* **4**(2), 490–530 (2005)
7. Candès, E.J., Romberg, J., Tao, T.: Robust uncertainty principles: Exact signal reconstruction from highly incomplete frequency information. *IEEE Transactions on information theory* **52**(2), 489–509 (2006)
8. Chung, H., Kim, J., McCann, M.T., Klasky, M.L., Ye, J.C.: Diffusion posterior sampling for general noisy inverse problems. *International Conference on Learning Representations* (2023)
9. Chung, H., Lee, S., Ye, J.C.: Decomposed diffusion sampler for accelerating large-scale inverse problems. *International Conference on Learning Representations* (2024)
10. Chung, H., Ryu, D., McCann, M.T., Klasky, M.L., Ye, J.C.: Solving 3d inverse problems using pre-trained 2d diffusion models. In: Proceedings of the IEEE/CVF conference on computer vision and pattern recognition. pp. 22542–22551 (2023)
11. Coupé, P., Yger, P., Prima, S., Hellier, P., Kervrann, C., Barillot, C.: An optimized blockwise nonlocal means denoising filter for 3-d magnetic resonance images. *IEEE transactions on medical imaging* **27**(4), 425–441 (2008)
12. Heckel, R., Hand, P.: Deep decoder: Concise image representations from untrained non-convolutional networks. *International Conference on Learning Representations* (2019)
13. Heckel, R., Soltanolkotabi, M.: Compressive sensing with un-trained neural networks: Gradient descent finds a smooth approximation. In: International conference on machine learning. pp. 4149–4158. PMLR (2020)
14. Ho, J., Jain, A., Abbeel, P.: Denoising diffusion probabilistic models. *Advances in neural information processing systems* **33**, 6840–6851 (2020)
15. Jia, F., Wong, W.H., Zeng, T.: Ddunet: Dense dense u-net with applications in image denoising. In: Proceedings of the IEEE/CVF international conference on computer vision. pp. 354–364 (2021)
16. Kremer, J.R., Mastronarde, D.N., McIntosh, J.R.: Computer visualization of three-dimensional image data using imod. *Journal of structural biology* **116**(1), 71–76 (1996)
17. Lee, S., Chung, H., Park, M., Park, J., Ryu, W.S., Ye, J.C.: Improving 3d imaging with pre-trained perpendicular 2d diffusion models. In: Proceedings of the IEEE/CVF international conference on computer vision. pp. 10710–10720 (2023)

18. Lehtinen, J., Munkberg, J., Hasselgren, J., Laine, S., Karras, T., Aittala, M., Aila, T.: Noise2noise: Learning image restoration without clean data. *International Conference on Machine Learning* (2018)
19. Lepcha, D.C., Goyal, B., Dogra, A., Vaghela, K., Singh, A., Kumar, K.R., Bavirisetti, D.P.: Low-dose computed tomography image denoising using pixel level non-local self-similarity prior with non-local means for healthcare informatics. *Scientific Reports* **15**(1), 25095 (2025)
20. Levandowsky, M., Winter, D.: Distance between sets. *Nature* **234**(5323), 34–35 (1971)
21. Li, X., Lu, J., Ding, H., Sun, C., Zhou, J.T., Chee, Y.M.: Pointcvar: Risk-optimized outlier removal for robust 3d point cloud classification. In: *Proceedings of the AAAI Conference on Artificial Intelligence*. vol. 38, pp. 21340–21348 (2024)
22. Pierazzo, N., Morel, J.M., Facciolo, G.: Multi-scale dct denoising. *Image Processing On Line* **7**, 288–308 (2017)
23. Rakotosaona, M.J., La Barbera, V., Guerrero, P., Mitra, N.J., Ovsjanikov, M.: Pointcleannet: Learning to denoise and remove outliers from dense point clouds. In: *Computer graphics forum*. vol. 39, pp. 185–203. Wiley Online Library (2020)
24. Saragadam, V., LeJeune, D., Tan, J., Balakrishnan, G., Veeraraghavan, A., Baraniuk, R.G.: Wire: Wavelet implicit neural representations. In: *Proceedings of the IEEE/CVF Conference on Computer Vision and Pattern Recognition*. pp. 18507–18516 (2023)
25. Sitzmann, V., Martel, J.N., Bergman, A.W., Lindell, D.B., Wetzstein, G.: Implicit neural representations with periodic activation functions. In: *Proc. NeurIPS* (2020)
26. Sivgin, I., Fridovich-Keil, S., Wetzstein, G., Pilanci, M.: Geometric algebra planes: Convex implicit neural volumes. In: *International Conference on Machine Learning* (2025)
27. Smith-Bindman, R., Chu, P.W., Firdaus, H.A., Stewart, C., Malekheadayat, M., Alber, S., Bolch, W.E., Mahendra, M., de González, A.B., Miglioretti, D.L.: Projected lifetime cancer risks from current computed tomography imaging. *JAMA internal medicine* **185**(6), 710–719 (2025)
28. Song, B., Duan, Z., Gao, Y., Shao, T.: Adaptive bm3d algorithm for image denoising using coefficient of variation. In: *2019 22th International Conference on Information Fusion (FUSION)*. pp. 1–8. IEEE (2019)
29. Song, B., Hu, J., Luo, Z., Fessler, J., Shen, L.: Diffusionblend: Learning 3D image prior through position-aware diffusion score blending for 3D computed tomography reconstruction. *Advances in Neural Information Processing Systems* **37**, 89584–89611 (2024)
30. Sun, Y., Schneider, L.S., Gu, M., Mei, S., Ye, C., Wagner, F., Bayer, S., Maier, A.: Filter2noise: Interpretable self-supervised single-image denoising for low-dose ct with attention-guided bilateral filtering. *arXiv preprint arXiv:2504.13519* (2025)
31. Tancik, M., Srinivasan, P., Mildenhall, B., Fridovich-Keil, S., Raghavan, N., Singhal, U., Ramamoorthi, R., Barron, J., Ng, R.: Fourier features let networks learn high frequency functions in low dimensional domains. *Advances in neural information processing systems* **33**, 7537–7547 (2020)
32. Turk, M., Baumeister, W.: The promise and the challenges of cryo-electron tomography. *FEBS letters* **594**(20), 3243–3261 (2020)
33. Ulyanov, D., Vedaldi, A., Lempitsky, V.: Deep image prior. In: *Proceedings of the IEEE conference on computer vision and pattern recognition*. pp. 9446–9454 (2018)
34. Verbin, D., Zickler, T.: Field of junctions: Extracting boundary structure at low snr. In: *Proceedings of the IEEE/CVF international conference on computer vision*. pp. 6869–6878 (2021)

35. Wang, Z., Bovik, A., Sheikh, H., Simoncelli, E.: Image quality assessment: from error visibility to structural similarity. *IEEE Transactions on Image Processing* **13**(4), 600–612 (2004). <https://doi.org/10.1109/TIP.2003.819861>
36. Xu, X., Chi, Y.: Provably robust score-based diffusion posterior sampling for plug-and-play image reconstruction. *Advances in Neural Information Processing Systems* **37**, 36148–36184 (2024)
37. Yang, G.J.: Median filters and their applications to image processing. Purdue University (1980)
38. Yang, Z., Zang, D., Li, H., Zhang, Z., Zhang, F., Han, R.: Self-supervised noise modeling and sparsity guided electron tomography volumetric image denoising. *Ultramicroscopy* **255**, 113860 (2024)
39. Yang, Z., Zhang, F., Han, R.: Self-supervised cryo-electron tomography volumetric image restoration from single noisy volume with sparsity constraint. In: *Proceedings of the IEEE/CVF International Conference on Computer Vision*. pp. 4056–4065 (2021)
40. Yu, G., Sapiro, G.: Dct image denoising: a simple and effective image denoising algorithm. *Image Processing On Line* **1**, 292–296 (2011)
41. Yu, R., Li, X., Bi, T.: Modelling and validation of lidar noise distribution in fog and rain. *Measurement* **229**, 114472 (2024)
42. Zha, R., Lin, T.J., Cai, Y., Cao, J., Zhang, Y., Li, H.: R<sup>2</sup>-gaussian: Rectifying radiative gaussian splatting for tomographic reconstruction. In: *Advances in Neural Information Processing Systems (NeurIPS)* (2024)
43. Zhu, W., Mousavi, S.M., Beroza, G.C.: Seismic signal denoising and decomposition using deep neural networks. *IEEE Transactions on Geoscience and Remote Sensing* **57**(11), 9476–9488 (2019)
44. Zhu, Y., Huang, C.: An improved median filtering algorithm for image noise reduction. *Physics Procedia* **25**, 609–616 (2012)
45. Zhu, Y., Zhang, K., Liang, J., Cao, J., Wen, B., Timofte, R., Gool, L.V.: Denoising diffusion models for plug-and-play image restoration. In: *IEEE Conference on Computer Vision and Pattern Recognition Workshops (NTIRE)* (2023)

## 7 Soft Region Representation in 2D FoJ

As described in Section 4, our 3D FoJ uses smooth indicator functions to define soft, differentiable region assignments and boundary maps. These are inspired by a similar differentiable formulation in 2D FoJ [34], which we describe here.

For each 2D patch, a set of signed distance functions is defined to measure the perpendicular distance of any pixel  $\mathbf{p} = (x, y)$  from the  $k$ th boundary line passing through the vertex  $\mathbf{p}_i^{(0)}$  at orientation  $\phi_i^{(k)}$ :

$$d_k(\mathbf{p}) = -(x - x_i^{(0)}) \sin \phi_i^{(k)} + (y - y_i^{(0)}) \cos \phi_i^{(k)}. \quad (17)$$

Similarly, for each pair of boundary lines  $k$  and  $l$ , the signed distance function is:

$$d_{kl}(\mathbf{p}) = \begin{cases} \min\{d_k(\mathbf{p}), -d_l(\mathbf{p})\}, & \text{if } \phi_i^{(l)} - \phi_i^{(k)} < \pi, \\ \max\{d_k(\mathbf{p}), -d_l(\mathbf{p})\}, & \text{otherwise.} \end{cases} \quad (18)$$

To create a differentiable indicator of junction structure, the binary wedge boundaries are replaced by differentiable functions based on a regularized Heaviside operator:

$$H_\eta(d) = \frac{1}{2} \left( 1 + \frac{2}{\pi} \arctan \frac{d}{\eta} \right), \quad (19)$$

where  $\eta > 0$  controls the smoothness of the transition between adjacent regions. For  $M = 3$ , the continuous region indicators are then given by

$$\begin{aligned} u_{\theta_i}^{(1)}(\mathbf{p}) &= 1 - H_\eta(d_{13}(\mathbf{p})), \\ u_{\theta_i}^{(2)}(\mathbf{p}) &= H_\eta(d_{13}(\mathbf{p})) [1 - H_\eta(d_{12}(\mathbf{p}))], \\ u_{\theta_i}^{(3)}(\mathbf{p}) &= H_\eta(d_{13}(\mathbf{p})) H_\eta(d_{12}(\mathbf{p})). \end{aligned} \quad (20)$$

Each function  $u_{\theta_i}^{(j)}(\mathbf{p}) \in [0, 1]$  varies smoothly across the boundary and approaches 1 inside region  $j$ . This relaxation ensures differentiability of the objective function in Equation (2) with respect to both the angular and positional parameters of each junction.

The binary boundary maps  $B_i(\mathbf{p})$  and  $\widehat{B}(\mathbf{p})$  in Equation (2) are likewise replaced by soft local and global boundary maps, defined using the gradients of the smooth indicator functions. The soft boundary map for patch  $i$  with  $M = 3$  is defined as

$$B_i^{(\delta)}(\mathbf{p}) = \pi \delta H'_\delta(\min\{|d_{12}(\mathbf{p})|, |d_{13}(\mathbf{p})|\}), \quad (21)$$

where  $H'_\delta$  denotes the derivative of  $H_\delta$  with respect to  $d$ , and  $\delta$  controls the effective width of the boundary transition. This continuous version approximates the binary boundary map while providing smoother gradients for optimization. The 2D FoJ paper [34] recommends using  $\eta=0.01$  and  $\delta=0.1$ , as these values yield sharp yet numerically stable transitions.

---

**Algorithm 1** 3D FoJ Optimization Procedure

---

**Input:** Volumetric data divided into 3D patches  $\{\mathbf{V}_i\}$ , number of patches  $N$ , number of planes  $L$  per junction (default  $L = 3$ ), number of regions  $M$  per junction (default  $M = 3$ ), initialization iterations  $N_{\text{init}}$ , refinement iterations  $N_{\text{refine}}$ , step size  $\lambda$

**Output:** Optimized junction parameters  $\gamma_i = (\boldsymbol{\rho}_i, \mathbf{v}_i^{(0)})$  and region intensities  $c_i^{(\ell)}$

1: **Initialization:**  
2: **for**  $i = 1, \dots, N$  **do**  
3:   Initialize offset  $\mathbf{v}_i^{(0)}$  at patch center  
4:   **for**  $t = 1, \dots, N_{\text{init}}$  **do**  
5:     **for**  $\ell = 1, \dots, L$  **do**  
6:        $(\theta_i^{(\ell)}, \phi_i^{(\ell)}) \leftarrow \arg \min_{\theta, \phi} \mathcal{L}_{\text{data}}(\theta, \phi)$   
7:     **end for**  
8:      $\mathbf{v}_i^{(0)} \leftarrow \arg \min_{\mathbf{v}} \mathcal{L}_{\text{data}}(\boldsymbol{\rho}_i, \mathbf{v})$   
9:   **end for**  
10: **end for**  
11: **Refinement:**  
12: **for**  $t = 1, \dots, N_{\text{refine}}$  **do**  
13:   Replace binary indicators  $u_{\gamma_i}^{(j)}$  and  $B_i$  with differentiable versions  $u_{\gamma_i, \eta}^{(j)}$ ,  $B_i^{(\delta)}$   
14:   **for**  $i = 1, \dots, N$  **do**  
15:     Update orientation and offset parameters via gradient-based optimization:  

$$\gamma_i \leftarrow \gamma_i - \lambda \nabla_{\gamma_i} \mathcal{L}_{\text{3D-FoJ}}$$
  
16:     Update region intensities analytically:  

$$c_i^{(j)} = \frac{\iiint u_{\gamma_i, \eta}^{(j)}(\mathbf{v}) [V_i(\mathbf{v}) + \lambda_C \widehat{V}(\mathbf{v})] d\mathbf{v}}{(1 + \lambda_C) \iiint u_{\gamma_i, \eta}^{(j)}(\mathbf{v}) d\mathbf{v}}$$
  
17:   **end for**  
18:   Gradually increase  $\lambda_B, \lambda_C$  in the loss function, to enforce boundary and color consistency  
19: **end for**

---

## 8 3D FoJ Optimization algorithm

A full step-by-step description of the 3D FoJ optimization procedure is provided in Algorithm 1.

## 9 Additional Results

In this section, we present extended qualitative and quantitative evaluations complementing the main results in the paper.

### 9.1 Low-dose X-ray Computed Tomography (CT)

Table 4 reports MS-SSIM measured on all 360° unseen projections (one projection per degree) and 3D PSNR measured on reconstructed volumes for every

dataset (*engine*, *foot*, *jaw*, *pepper*, and *teapot*) and noise level (*P50*, *P100*, and *P1000*). Across volumes and noise levels, 3D FoJ consistently achieves the highest 2D MS-SSIM and 3D PSNR. Competing baselines (3D-TV, R<sup>2</sup>-Gaussian [42], Filter2Noise [30]) either over-smooth boundaries or fail to recover region-consistent intensities, leading to lower fidelity especially under the most severe noise level (*P50*).

Figure 6 Figure 7, and Figure 8 visualize unseen projection views synthesized from the reconstructed 3D volumes at noise levels *P50*, *P100*, and *P1000*, respectively. Across all datasets, 3D FoJ consistently recovers sharper boundaries, more accurate object contours, and fewer noise-induced artifacts. In contrast, R<sup>2</sup>-Gaussian and Filter2Noise often lose fine structural details, particularly under low-SNR conditions, while 3D-TV tends to over-smooth textures, resulting in blurred edges and degraded object shape. Insets further demonstrate that FoJ preserves structure while effectively suppressing noise.

Figure 9, Figure 10, and Figure 11 present axial, sagittal, and coronal slices of reconstructed 3D volumes across datasets, at noise levels *P50*, *P100*, and *P1000*, respectively. 3D FoJ preserves boundaries, interfaces, and material transitions more consistently than other methods, while R<sup>2</sup>-Gaussian fails to recover a 3D volume for most of the datasets, instead overfitting to the limited projection views. TV-based reconstructions exhibit characteristic blocky artifacts and detail loss, while Filter2Noise reduces noise but simultaneously removes fine boundaries. Altogether, these slice views demonstrate that 3D FoJ provides a more faithful reconstruction of internal anatomy and geometry, even under highly degraded sparse-view and extremely low-dose CT conditions.

## 9.2 Cryogenic Electron Tomography (cryo-ET)

We provide additional qualitative denoising results for three real cryo-ET datasets—*mitochondria*, *vesicle*, and *VEEV*—in Figure 12. As in the main paper, all methods operate directly on the noisy 3D reconstructions, which contain both strong Poisson noise from low electron dose and missing-wedge artifacts from limited tilt angles. Because clean ground-truth volumes and raw tilt-series are unavailable, we focus on visual comparisons of structural fidelity across methods.

Across all three datasets, 3D FoJ produces the best trade-off between noise removal, contrast enhancement, and preservation of fine structures. In the *mitochondria* volume, 3D FoJ sharpens inner and outer mitochondrial membranes, whereas SC-Net [39] and NLM [5] over-smooth these thin membranes and suppress low-contrast internal detail. For the *vesicle* volume, 3D FoJ enhances vesicle boundaries and resolves small sub-vesicular structures while suppressing the granular background noise that remains in the input and NLM outputs. For the *VEEV* dataset, 3D FoJ recovers a clear, smooth viral boundary while simultaneously enhancing the thin, elongated groove-like structure in the upper-left region of the slice. This feature is faint and partially obscured in the noisy input and NLM outputs, and SC-Net tends to over-smooth it together with the surrounding membrane. In contrast, 3D FoJ preserves the narrow linear indentation with high contrast, revealing its full shape. This example highlights the ability of

3D FoJ to recover subtle, low-contrast morphological details. Together with the *centriole* results shown in the main paper, these examples indicate that 3D FoJ can reliably denoise real cryo-ET volumes while preserving delicate biological morphology in the absence of ground-truth supervision.

### 9.3 Point Cloud Denoising

We show the behavior of each method across 28 point cloud datasets under two noise settings: outlier noise and spread noise. The comparison metric is Chamfer-L2 error; results are reported in Tables 5 and 6.

In the outlier-noise setting, 3D FoJ achieves the lowest Chamfer-L2 error on every dataset and at every outlier ratio (10%, 30%, 60%, 90%). While PointCVaR [21] and PointCleanNet [23] show competitive performance at low outlier ratios, their fidelity degrades substantially as the proportion of outliers grows. Nonlocal means (NLM) [5] exhibits similar degradation under high noise. In contrast, 3D FoJ preserves accurate shape even at the highest outlier levels.

We can observe a similar trend in the spread-noise setting. Across all four noise levels (40k, 100k, 200k, 500k), 3D FoJ maintains the lowest or near-lowest Chamfer-L2 error across different shapes. PointCVaR performs competitively at the 100k noise level, but its errors rise at higher noise levels. PointCleanNet and NLM also display a consistent increase in error as noise increases. In comparison, 3D FoJ exhibits significantly lower error even under the highest noise, showing robustness across all spread-noise conditions.

Overall, these quantitative results demonstrate that 3D FoJ provides the most stable point cloud denoising performance across both outlier and spread noise models and all noise levels, with consistently lower Chamfer-L2 errors than the competing methods.

### 9.4 Ablation Study

Figure 13 and Table 7 study how the number of regions and the number of initialization and refinement iterations influence reconstruction fidelity. The results show that increasing the number of initialization and refinement iterations does not improve reconstruction quality. In fact, the highest MS-SSIM and 3D PSNR values are consistently achieved with the smallest number of iterations.

Varying the number of regions also shows a clear trend: using 2–4 regions provides good performance, while increasing the region count beyond this tends to introduce unnecessary model complexity without improving accuracy. Higher region counts slightly increase runtime (due to larger parameter sets).

Overall, the ablation confirms that a small number of iterations and a moderate number of regions (2–4) provides the best balance between reconstruction quality and computational efficiency.

Metric	Dataset	Method	P50	P100	P1000
2D MS-SSIM	<i>pepper</i>	3D-TV	0.665	0.679	0.733
		R <sup>2</sup> -Gaussian	0.593	0.593	0.593
		Filter2Noise	0.665	0.745	0.745
		3D FoJ (ours)	0.698	0.736	0.780
	<i>teapot</i>	3D-TV	0.668	0.747	0.939
		R <sup>2</sup> -Gaussian	0.692	0.692	0.651
		Filter2Noise	0.534	0.547	0.531
		3D FoJ (ours)	0.757	0.811	0.882
	<i>jaw</i>	3D-TV	0.883	0.899	0.904
		R <sup>2</sup> -Gaussian	0.350	0.350	0.350
		Filter2Noise	0.857	0.848	0.832
		3D FoJ (ours)	0.917	0.914	0.912
	<i>foot</i>	3D-TV	0.571	0.596	0.706
		R <sup>2</sup> -Gaussian	0.608	0.608	0.608
		Filter2Noise	0.595	0.622	0.684
		3D FoJ (ours)	0.630	0.660	0.704
	<i>engine</i>	3D-TV	0.727	0.772	0.863
		R <sup>2</sup> -Gaussian	0.629	0.642	0.653
		Filter2Noise	0.661	0.681	0.681
		3D FoJ (ours)	0.766	0.820	0.911
3D PSNR	<i>pepper</i>	3D-TV	8.65	10.92	13.86
		R <sup>2</sup> -Gaussian	13.48	13.48	13.48
		Filter2Noise	6.93	13.42	13.42
		3D FoJ (ours)	12.13	12.54	13.49
	<i>teapot</i>	3D-TV	19.90	20.72	21.16
		R <sup>2</sup> -Gaussian	18.55	18.55	17.50
		Filter2Noise	16.38	18.20	11.15
		3D FoJ (ours)	20.45	20.69	21.18
	<i>jaw</i>	3D-TV	18.64	19.09	19.00
		R <sup>2</sup> -Gaussian	12.55	12.55	12.55
		Filter2Noise	12.93	14.19	15.70
		3D FoJ (ours)	18.74	18.81	19.00
	<i>foot</i>	3D-TV	14.40	15.84	16.71
		R <sup>2</sup> -Gaussian	15.26	15.26	15.26
		Filter2Noise	11.87	13.74	16.80
		3D FoJ (ours)	15.60	15.79	16.15
	<i>engine</i>	3D-TV	7.37	9.96	14.08
		R <sup>2</sup> -Gaussian	16.61	16.61	16.63
		Filter2Noise	9.93	16.11	16.11
		3D FoJ (ours)	12.49	12.86	13.77

**Table 4:** MS-SSIM measured on 2D projections across the full 360° range and 3D PSNR measured on 3D volumes across all CT datasets for each noise level. 3D FoJ produces the highest-fidelity reconstructions, especially at low SNR (*P50*).

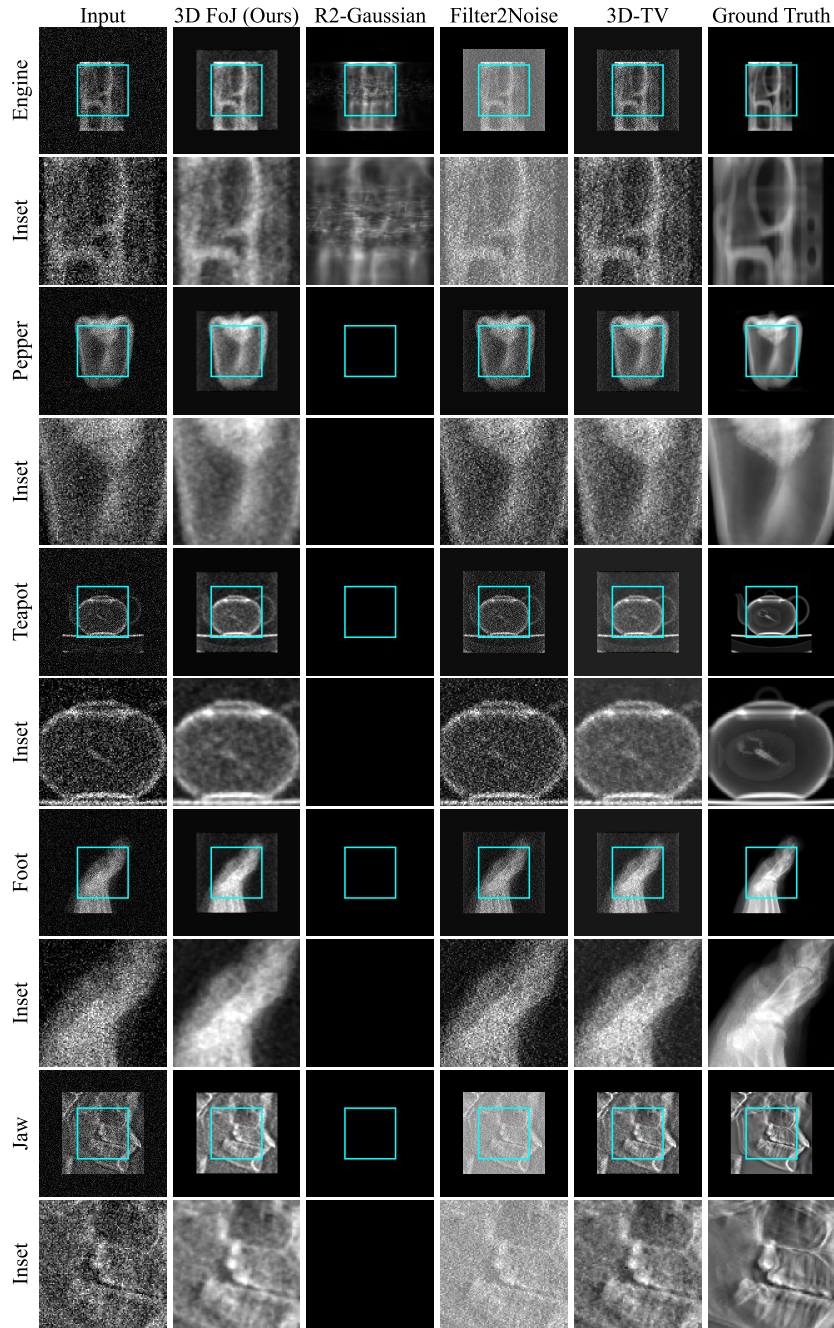


**Fig. 6:** Comparison of unseen projection views synthesized from reconstructed 3D volumes for all datasets under low-SNR ( $P50$ ) conditions.

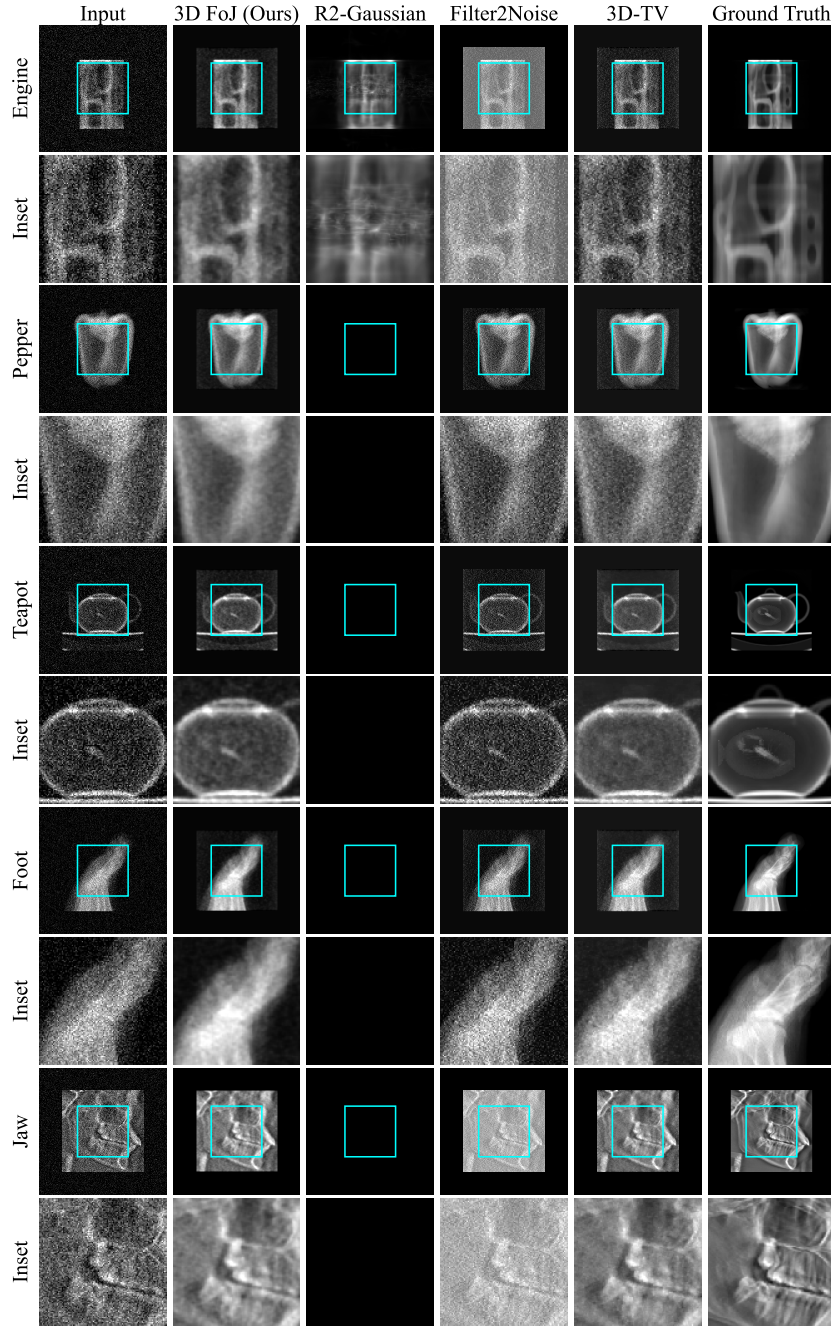


**Fig. 7:** Comparison of unseen projection views synthesized from reconstructed 3D volumes for all datasets under medium-SNR ( $P100$ ) conditions.

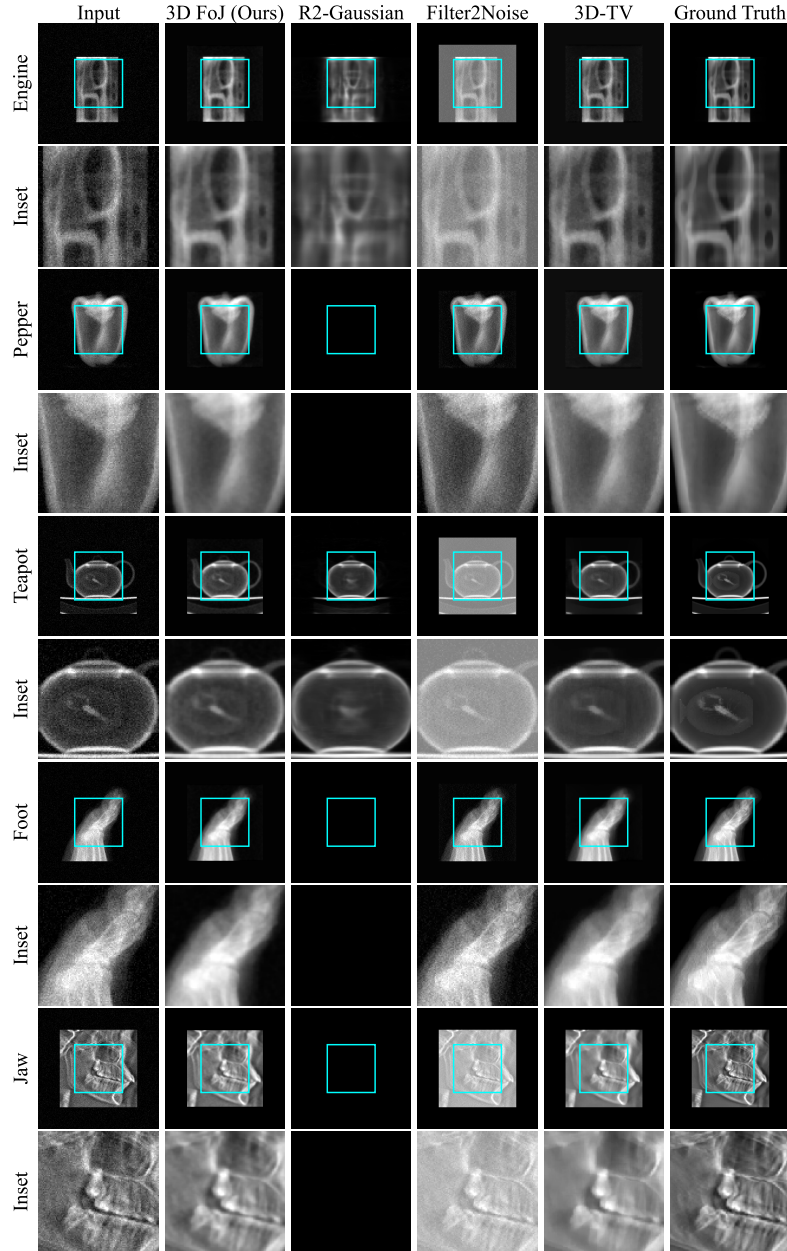


**Fig. 8:** Comparison of unseen projection views synthesized from reconstructed 3D volumes for all datasets under high-SNR ( $P1000$ ) conditions.

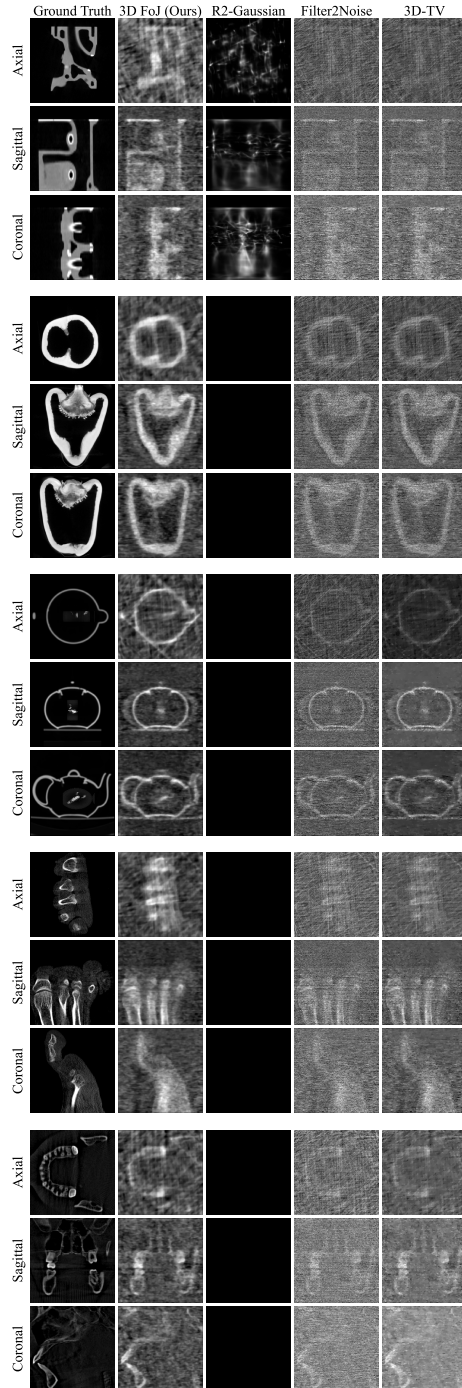


**Fig. 9:** Comparison of slice views of reconstructed 3D volumes for all datasets under low-SNR ( $P50$ ) conditions.

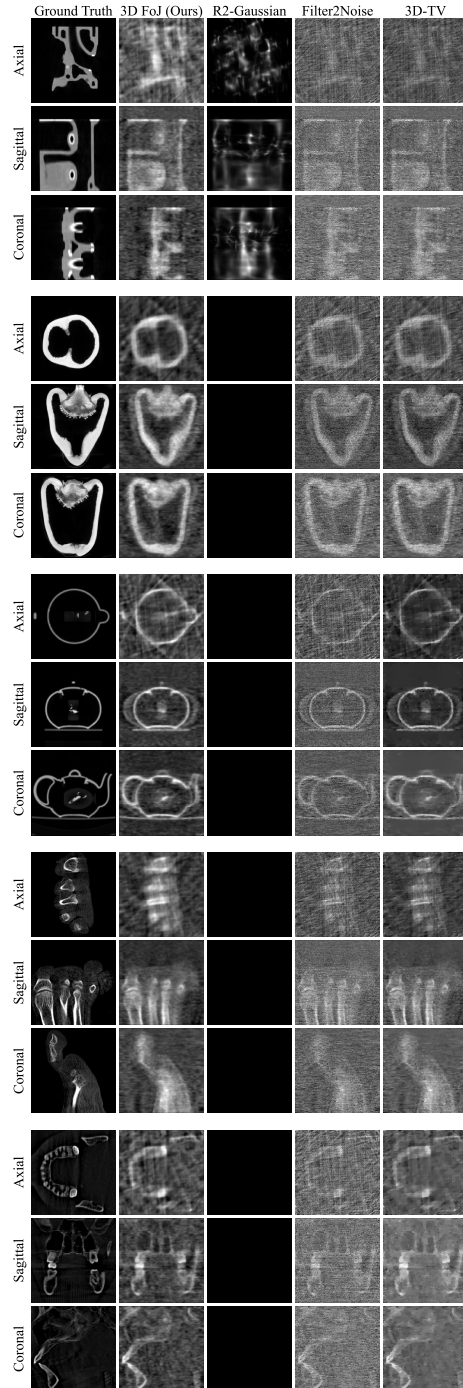


**Fig. 10:** Comparison of slice views of reconstructed 3D volumes for all datasets under medium-SNR ( $P100$ ) conditions.

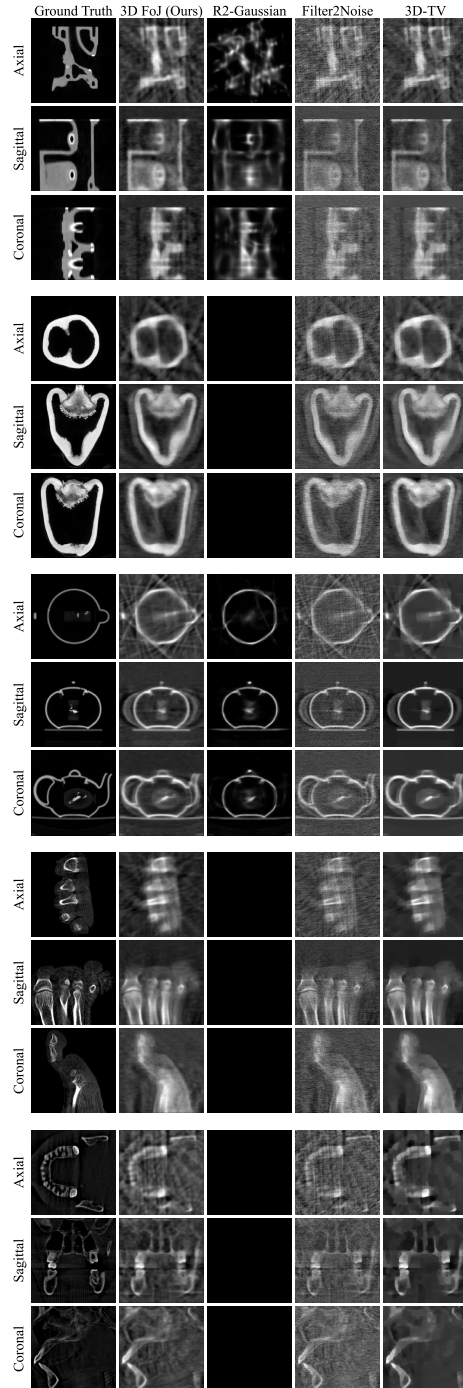


**Fig. 11:** Comparison of slice views of reconstructed 3D volumes for all datasets under high-SNR ( $P1000$ ) conditions.

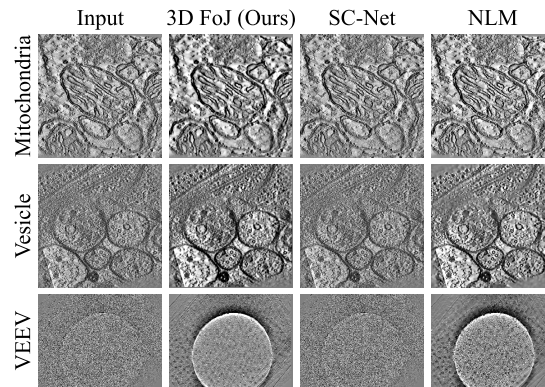


**Fig. 12:** Additional visual denoising results for the real cryo-ET *Mitochondria*, *Vesicle*, and VEEV volumes, sliced in the  $y$  dimension. 3D FoJ enhances membrane contrast and resolves fine structural details while reducing noise, compared with the input, SC-Net [39], and nonlocal means (NLM) [5]

Dataset	Noise Level 10%				Noise Level 30%			
	PointCvAr	PointCleanNet	NLM	3D FoJ	PointCvAr	PointCleanNet	NLM	3D FoJ
Cup33	0.0014	0.0020	0.0018	0.0001	0.0050	0.0060	0.0058	0.0001
LegoLeg	0.0016	0.0017	0.0017	0.0001	0.0051	0.0052	0.0051	0.0001
Liberty	0.0296	0.0322	0.1299	0.0015	0.0925	0.0964	0.1466	0.0016
LibertyBase	0.0024	0.0026	0.0020	0.0002	0.0074	0.0077	0.0062	0.0003
armadillo	17.4917	17.4023	41.1563	1.0438	53.2626	53.0428	60.0359	1.0914
box_groove	0.0468	0.0553	0.0159	0.0047	0.1531	0.1650	0.0760	0.0120
box_push	0.0730	0.0797	0.0729	0.0055	0.2298	0.2396	0.2363	0.0062
boxunion2	0.0032	0.0047	0.0045	0.0003	0.0116	0.0140	0.0135	0.0003
boxunion_uniform	0.0023	0.0032	0.0009	0.0003	0.0081	0.0095	0.0060	0.0003
bunny	0.0067	0.0080	0.0079	0.0004	0.0223	0.0242	0.0241	0.0005
column	3.5018	3.4981	8.8556	0.2346	10.2025	10.6478	13.0056	0.1701
column_head	0.2254	0.2231	0.1915	0.0463	0.6704	0.6673	0.5965	0.0522
cube_uniform	0.0006	0.0009	0.0002	0.0001	0.0023	0.0027	0.0009	0.0001
cylinder	0.0027	0.0038	0.0023	0.0002	0.0097	0.0114	0.0072	0.0003
dragon	0.0000	0.0000	0.0000	0.0000	0.0001	0.0001	0.0001	0.0000
dragon_xyzrgb	30.9469	30.7425	82.1093	1.7697	92.1006	91.3520	118.2381	1.8064
fanDisk	0.0194	0.0212	0.0208	0.0011	0.0604	0.0631	0.0664	0.0011
flower	0.8129	0.9397	1.0486	0.0504	2.6427	2.8260	3.3228	0.0537
galera	0.0163	0.0166	0.0169	0.0011	0.0497	0.0500	0.0518	0.0011
happy	0.0000	0.0000	0.0001	0.0000	0.0001	0.0001	0.0001	0.0000
icosahedron	0.0019	0.0027	0.0023	0.0001	0.0070	0.0082	0.0074	0.0002
netsuke	2.8787	2.8236	2.9063	0.1953	8.6102	8.5556	9.1302	0.1844
pipe	0.0150	0.0168	0.0173	0.0010	0.0478	0.0506	0.0513	0.0010
pipe_curve	0.0168	0.0184	0.0197	0.0012	0.0527	0.0551	0.0576	0.0012
star_halfsmooth	0.0074	0.0075	0.0078	0.0004	0.0225	0.0228	0.0261	0.0004
star_smooth	0.0037	0.0046	0.0048	0.0003	0.0123	0.0139	0.0152	0.0003
tortuga	0.0031	0.0033	0.0060	0.0002	0.0097	0.0101	0.0126	0.0002
yoda	4.0502	4.9398	3.8923	0.8875	14.6877	14.6165	13.9355	1.0102

Dataset	Noise Level 60%				Noise Level 90%			
	PointCvAr	PointCleanNet	NLM	3D FoJ	PointCvAr	PointCleanNet	NLM	3D FoJ
Cup33	0.0109	0.0120	0.0110	0.0002	0.0170	0.0181	0.0163	0.0030
LegoLeg	0.0103	0.0104	0.0095	0.0001	0.0155	0.0157	0.0137	0.0014
Liberty	0.1877	0.1930	0.2124	0.0032	0.2866	0.2906	0.2717	0.0205
LibertyBase	0.0152	0.0157	0.0118	0.0006	0.0232	0.0237	0.0175	0.0100
armadillo	106.0517	106.0869	103.7139	1.2459	160.9545	160.5282	145.6340	8.4291
box_groove	0.3154	0.3303	0.1476	0.0178	0.4852	0.4989	0.2250	0.1640
box_push	0.4662	0.4777	0.4372	0.0105	0.7112	0.7199	0.6439	0.1695
boxunion2	0.0257	0.0281	0.0250	0.0004	0.0398	0.0424	0.0364	0.0063
boxunion_uniform	0.0174	0.0190	0.0150	0.0004	0.0270	0.0285	0.0221	0.0071
bunny	0.0459	0.0479	0.0432	0.0007	0.0704	0.0722	0.0617	0.0108
column	20.8850	21.1058	21.7367	0.2624	31.8108	31.6407	28.8462	2.6576
column_head	1.3346	1.3331	1.1293	0.0692	2.0186	2.0092	1.6877	0.4316
cube_uniform	0.0049	0.0055	0.0023	0.0003	0.0077	0.0082	0.0036	0.0022
cylinder	0.0206	0.0227	0.0137	0.0009	0.0321	0.0341	0.0207	0.0104
dragon	0.0001	0.0002	0.0002	0.0000	0.0002	0.0002	0.0002	0.0000
dragon_xyzrgb	181.3145	180.7101	197.2864	2.5481	273.3175	271.9570	263.5173	29.7845
fanDisk	0.1228	0.1260	0.1177	0.0012	0.1878	0.1910	0.1690	0.0175
flower	5.4071	5.6100	5.7536	0.0639	8.2968	8.4817	7.9777	0.5627
galera	0.0997	0.1002	0.0954	0.0013	0.1503	0.1502	0.1356	0.0149
happy	0.0001	0.0002	0.0002	0.0000	0.0002	0.0003	0.0002	0.0000
icosahedron	0.0151	0.0166	0.0138	0.0003	0.0237	0.0250	0.0203	0.0074
netsuke	17.2499	17.2595	16.4935	0.2323	26.0029	25.9334	23.4266	2.1315
pipe	0.0980	0.1016	0.0927	0.0015	0.1492	0.1527	0.1309	0.0150
pipe_curve	0.1078	0.1109	0.1053	0.0017	0.1628	0.1659	0.1466	0.0233
star_halfsmooth	0.0451	0.0456	0.0466	0.0004	0.0682	0.0685	0.0655	0.0068
star_smooth	0.0274	0.0277	0.0276	0.0003	0.0415	0.0417	0.0393	0.0032
tortuga	0.0198	0.0201	0.0213	0.0002	0.0299	0.0302	0.0287	0.0012
yoda	28.1077	29.6142	27.8578	1.7628	44.9544	44.8306	40.5248	4.3073

**Table 5:** ChamferL2 comparison under the outlier noise settings {10%, 30%, 60%, 90%}. 3D FoJ achieves the lowest error across all datasets and remains stable even as the outlier ratio increases. Other methods show rapidly increasing errors at higher noise levels, especially on complex shapes such as armadillo, dragon, and flower, while 3D FoJ preserves geometry with only a small change in error. Overall, 3D FoJ provides the most reliable reconstruction quality across all outlier noise levels.

Dataset	Noise Level 40000				Noise Level 100000			
	PointCVaR	PointCleanNet	NLM	3D FoJ	PointCVaR	PointCleanNet	NLM	3D FoJ
Cup33	30.9605	0.0248	0.0293	0.0001	1.7726	0.0435	0.0483	0.0002
LegoLeg	30.3808	0.0304	0.0372	0.0001	0.0000	0.0532	0.0604	0.0001
Liberty	40.4311	1.2590	2.2693	0.0015	0.0117	2.2111	3.1473	0.0014
LibertyBase	28.3421	0.0100	0.0113	0.0002	0.0878	0.0175	0.0188	0.0002
armadillo	525.1897	377.7829	503.1765	1.0885	0.0000	660.6212	796.6649	1.1087
box_groove	21.3624	0.2838	0.3158	0.0062	0.0000	0.4977	0.5290	0.0056
box_push	28.3982	0.3628	0.4220	0.0058	0.0000	0.6338	0.6988	0.0057
boxunion2	30.6402	0.0547	0.0663	0.0003	1.5264	0.0962	0.1092	0.0003
boxunion_uniform	29.5142	0.0207	0.0239	0.0003	1.4309	0.0364	0.0397	0.0003
bunny	30.9756	0.1229	0.1526	0.0005	1.3982	0.2131	0.2464	0.0004
column	514.2000	141.3988	196.5365	0.1645	0.0000	247.0045	326.9531	0.1643
column_head	30.4894	1.9100	2.0876	0.0410	0.0000	3.3705	3.5892	0.0439
cube_uniform	28.9115	0.0056	0.0062	0.0001	1.9634	0.0098	0.0104	0.0001
cylinder	28.4080	0.0212	0.0243	0.0002	1.1429	0.0376	0.0408	0.0002
dragon	30.1898	0.0008	0.0011	0.0000	0.7854	0.0014	0.0017	0.0000
dragon_xyzrgb	2094.9787	972.3282	1438.1343	1.6082	0.0000	1687.3487	2253.5707	1.7542
fanisk	32.0970	0.4419	0.5664	0.0011	0.0000	0.7744	0.9097	0.0011
flower	85.8532	20.9525	27.6863	0.0465	0.0000	36.3354	43.6728	0.0510
galera	33.0891	0.3065	0.3777	0.0011	0.0000	0.5393	0.6196	0.0012
happy	30.2999	0.0010	0.0014	0.0000	0.7180	0.0018	0.0022	0.0000
icosahedron	30.4123	0.0186	0.0219	0.0001	1.3710	0.0325	0.0361	0.0002
netsuke	137.3421	68.2139	85.3554	0.1837	0.0000	119.0337	137.7499	0.2154
pipe	35.1910	0.5018	0.6291	0.0010	0.0000	0.8755	1.0136	0.0010
pipe_curve	34.7353	0.4732	0.5875	0.0012	0.0000	0.8271	0.9479	0.0014
star_halfsmooth	27.1354	0.0694	0.0902	0.0004	0.0000	0.1215	0.1447	0.0004
star_smooth	27.9685	0.0360	0.0446	0.0003	0.0016	0.0626	0.0718	0.0003
tortuga	31.6051	0.0721	0.1000	0.0002	0.0000	0.1260	0.1586	0.0002
yoda	294.4679	158.4453	178.6378	1.2085	0.0000	277.1665	296.8689	1.3129

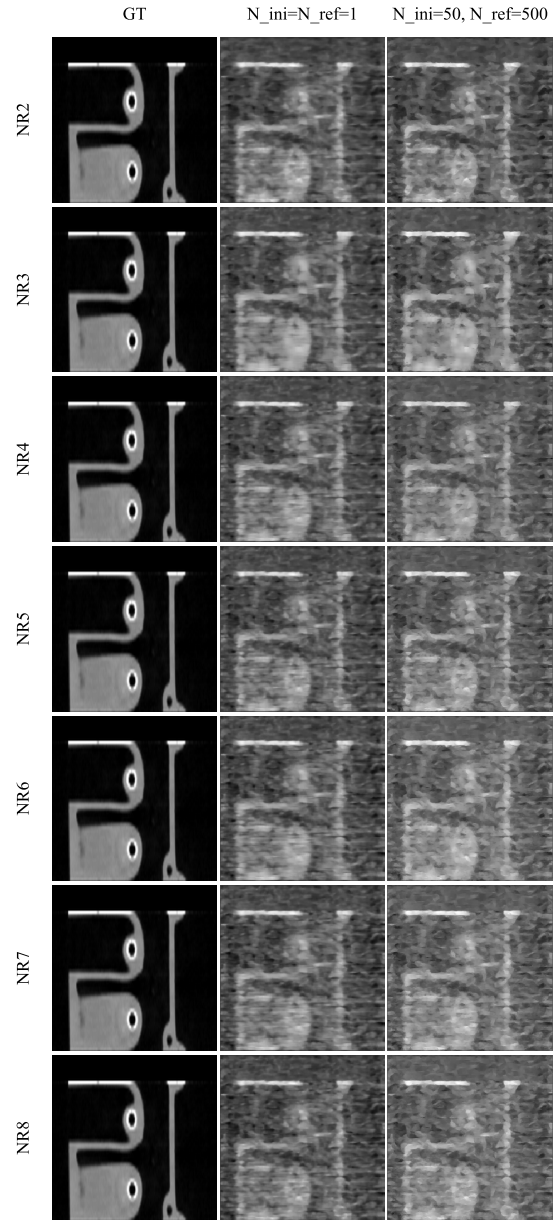
  

Dataset	Noise Level 200000				Noise Level 500000			
	PointCVaR	PointCleanNet	NLM	3D FoJ	PointCVaR	PointCleanNet	NLM	3D FoJ
Cup33	51.2295	0.0581	0.0616	0.0002	101.6741	0.0730	0.0757	0.0003
LegoLeg	50.1370	0.0711	0.0773	0.0001	102.0256	0.0889	0.0828	0.0001
Liberty	66.7135	2.9550	3.6719	0.0015	135.8302	3.6894	3.6443	0.0017
LibertyBase	46.7883	0.0232	0.0244	0.0002	94.8299	0.0289	0.0039	0.0004
armadillo	869.0288	879.8691	987.8753	1.1186	1737.7334	1098.1857	438.2211	1.3077
box_groove	35.8121	0.6634	0.6907	0.0057	71.6800	0.8265	0.7507	0.0076
box_push	47.4676	0.8404	0.8982	0.0064	96.6765	1.0576	0.1881	0.0074
boxunion2	50.5676	0.1287	0.1395	0.0003	101.2901	0.1606	0.0429	0.0004
boxunion_uniform	48.7418	0.0486	0.0519	0.0003	97.0436	0.0606	0.0106	0.0004
bunny	51.0638	0.2854	0.3128	0.0005	102.1750	0.3560	0.0628	0.0006
column	844.1674	329.7473	392.9127	0.1895	1704.4415	411.7895	407.2683	0.1811
column_head	50.7623	4.4689	4.6424	0.0436	101.7552	5.5979	0.7142	0.0422
cube_uniform	47.7497	0.0132	0.0104	0.0001	95.0206	0.0164	0.0155	0.0002
cylinder	47.4803	0.0497	0.0514	0.0003	94.9279	0.0623	0.0570	0.0004
dragon	49.6818	0.0019	0.0021	0.0000	100.2598	0.0023	0.0009	0.0000
dragon_xyzrgb	3503.9741	2259.3765	2696.7554	1.9382	7024.6872	2825.4123	1740.8934	2.0648
fanisk	53.4734	1.0400	1.1499	0.0012	108.1353	1.2981	0.4451	0.0014
flower	142.6379	48.5886	54.8414	0.0580	286.3444	60.5215	24.6729	0.0664
galera	55.2452	0.7166	0.7792	0.0012	110.0765	0.8965	0.2512	0.0017
happy	49.9020	0.0024	0.0027	0.0000	100.2257	0.0030	0.0029	0.0000
icosahedron	49.7841	0.0437	0.0466	0.0002	98.9937	0.0545	0.0373	0.0003
netsuke	230.1374	159.0817	174.4530	0.2249	460.2821	198.9867	70.7092	0.3166
pipe	58.2976	1.1654	1.2764	0.0010	116.7092	1.4471	1.2878	0.0015
pipe_curve	57.9949	1.1040	1.2031	0.0014	116.2264	1.3836	1.2681	0.0019
star_halfsmooth	44.8887	0.1615	0.1800	0.0004	91.1262	0.2022	0.0891	0.0005
star_smooth	46.4555	0.0831	0.0908	0.0003	93.8240	0.1047	0.0397	0.0004
tortuga	52.3346	0.1681	0.1937	0.0002	105.8191	0.2099	0.0967	0.0002
yoda	485.5565	367.5865	383.9735	1.4843	977.1352	458.9167	188.5749	9.4823

**Table 6:** ChamferL2 comparison under the spread noise settings  $\{40k, 100k, 200k, 500k\}$ . 3D FoJ achieves the lowest error on most datasets and remains stable even at the highest noise levels. PointCVaR performs particularly well at the 100k noise level and can occasionally match or slightly outperform 3D FoJ on a few datasets, but its performance drops noticeably as noise increases further. Overall, 3D FoJ is the most consistent and robust method across the full range of spread noise levels.

$N_{\text{init}}$	$N_{\text{refine}}$	# regions	Batch size	Stride	Patch size	MS-SSIM	3D PSNR	Runtime
1	1	2	6	2	10	0.8048	17.025	15.2 min
1	1	3	6	2	10	0.7982	17.173	17.2 min
1	1	4	6	2	10	0.7975	16.701	20.3 min
1	1	5	6	2	10	0.7965	16.428	21.5 min
1	1	6	6	2	10	0.7897	16.502	22.8 min
1	1	7	6	2	10	0.7985	16.373	25.1 min
1	1	8	6	2	10	0.7969	16.124	27.7 min
50	500	2	1	2	10	0.7423	16.361	952 min
50	500	3	1	2	10	0.7008	16.184	1188 min
50	500	4	1	2	10	0.7290	16.015	1322.4 min
50	500	5	1	2	10	0.7560	15.836	1456 min
50	500	6	1	2	10	0.7267	15.958	1588.8 min
50	500	7	1	2	10	0.7561	15.842	1707.5 min
50	500	8	1	2	10	0.7578	15.688	1870.5 min

**Table 7:** Ablation study evaluating the effect of initialization steps, refinement iterations, and number of regions in 3D FoJ on the *engine* CT dataset under the highest noise level ( $P50$ ).



**Fig. 13:** Sagittal slice views of reconstructed 3D volumes from the *engine* dataset under low-SNR ( $P50$ ) conditions, illustrating the ablation study on the number of initialization steps, refinement iterations, and regions used in 3D FoJ.